ChemPubSoc Europe

DOI: 10.1002/cphc.201400063

Linker Rectifiers for Covalent Attachment of Transition-Metal Catalysts to Metal-Oxide Surfaces

Wendu Ding,[a, b] Christian F. A. Negre,[a, b] Julio L. Palma,[a] Alec C. Durrell,[a, b] Laura J. Allen,[a] Karin J. Young,[a] Rebecca L. Milot,[a] Charles A. Schmuttenmaer,*[a, b] Gary W. Brudvig,*[a, b] Robert H. Crabtree,*[a, b] and Victor S. Batista*[a, b]

The authors are grateful to Professor Michael Graetzel, who has been an inspirational figure in solar energy research

Linkers that favor rectification of interfacial electron transfer are likely to be required for efficient photo-driven catalysis of multi-electron reactions at electrode surfaces. Design principles are discussed, together with the synthesis and characterization of a specific pair of molecular linkers, related by inversion of the direction of an amide bond in the heart of the molecule. The linkers have a terpyridyl group that can covalently bind Mn as in a well-known water oxidation catalyst and an acetylacetonate group that allows attachment to TiO_2 surfaces. The appropriate choice of the sense of the amide linkage yields directionality of interfacial electron transfer, essential to enhance electron injection and slow back-electron transfer. Support comes from electron paramagnetic resonance and terahertz spectroscopic measurements, as well as computational modeling characterizing the asymmetry of electron transfer properties.

1. Introduction

The development of inexpensive and resilient photocatalytic solar cells for water splitting into H_2 and O_2 could offer a viable solution to the renewable energy challenge.[1–3] In this way, water would be used as a renewable feedstock of protons and electrons for a self-sustaining cycle. The outstanding challenge, however, is achieving efficient coupling of multiple one-electron, one-photon processes with the four-electron water oxidation reaction [Eq. (1)]:

$$2\,H_2O \rightarrow O_2 + 4\,e^- + 4\,H^+ \qquad (1)$$

Nature accomplishes such coupling during photosynthesis by rectification of photoinduced electron transfer (ET) through a series of redox cofactors embedded in photosystem II.[4,5] The resulting kinetically favored ET pathway leads to long-lived reduction of plastoquinone, which prevails over back ET (i.e. recombination) that is thermodynamically favored. Therefore, it is reasonable to expect that biomimetic photo-driven catalysis of multi-electron reactions at electrode surfaces will likely require rectification of interfacial electron transfer (IET).[6–8] This paper analyzes molecular linkers for covalent attachment of catalysts to metal-oxide electrode surfaces,[9–12] with emphasis on the structural features necessary to induce directionality of IET.

Titanium dioxide (TiO_2) is an attractive material for light-driven water splitting because the valence and conduction band edges bracket the water redox potentials,[13,14] although the valence band is just barely negative of H^+ reduction. Direct valence to conduction band transitions, however, require UV light, comprising $<4\%$ of the solar spectrum.[15] To shift the absorbance into the visible region, TiO_2 nanoparticles may be doped[16,17] or otherwise functionalized via surface modification by covalent attachment of molecular chromophores. These adsorbates can be used as molecular linkers to immobilize catalysts to the electrode surface.[6] Upon photooxidation by IET, the linkers can activate the attached molecular catalysts through multiple one electron, one photon, oxidative processes. However, undesired pathways might limit the overall efficiency of photoconversion and catalyst activation by IET. In particular, rapid decay of the excited state chromophore and recombination of the injected electron by reduction of the photooxidized sensitizer, or redox species in close contact with the surface, are typically competitive.[18,19] Therefore, it is essential to develop molecular linkers that induce directionality of IET and disfavor recombination.

Molecular rectification has been extensively explored in the field of molecular electronics,[20–22] and has been typically as-

[a] *W. Ding, Dr. C. F. A. Negre, Dr. J. L. Palma, Dr. A. C. Durrell, Dr. L. J. Allen, Dr. K. J. Young, R. L. Milot, Prof. C. A. Schmuttenmaer, Prof. G. W. Brudvig, Prof. R. H. Crabtree, Prof. V. S. Batista*
Chemistry Department, Yale University
225 Prospect Street, New Haven
CT 06520-8107 (USA)
E-mail: victor.batista@yale.edu
gary.brudvig@yale.edu
robert.crabtree@yale.edu
charles.schmuttenmaer@yale.edu

[b] *W. Ding, Dr. C. F. A. Negre, Dr. A. C. Durrell, Prof. C. A. Schmuttenmaer, Prof. G. W. Brudvig, Prof. R. H. Crabtree, Prof. V. S. Batista*
Energy Sciences Institute, Yale University
P.O. Box 27394, West Haven
Connecticut, 06516-7394 (USA)

Supporting Information for this article is available on the WWW under http://dx.doi.org/10.1002/cphc.201400063.

sessed in terms of the asymmetry of the forward and reverse currents upon changing the external voltage polarity applied to a molecular junction. Aviram and Ratner[20] first introduced the concept of unimolecular rectifiers in 1974 with a molecule that consisted of electron donor and electron acceptor rings bridged by σ-bonds. Since then, significant progress has been reported due to experimental breakthroughs in synthesis using self-assembly techniques, advanced micro-fabrication,[23–26] and electronic conductivity measurements performed by scanning probe microscopy[27] and break junction techniques.[28] However, applications of molecular rectifiers as linker-chromophores in dye-sensitized and photocatalytic cells have yet to be reported.

Extending our previous studies of molecular linkers for covalently attaching Mn complexes to TiO_2 surfaces,[6,9] we now explore structure/function relations responsible for inducing rectification. Comparison of our light-absorbing linkers, **Mn-terpy-L1-acac** and **Mn-terpy-L2-acac**, which differ only in the direction of the amide bond (Figure 1), suggest that **Mn-terpy-L2-acac** exhibits rectification and preferentially allows electrons to flow from the phenyl-acac moiety towards the Mn-terpy core, preventing long-lived photooxidation of Mn^{II} to Mn^{III}.[29] We analyze the role of the amide bridge linkage and its influence on electronic and structural features that provide a directionality to IET, which is essential to enhance electron injection into the TiO_2 conduction band and prevent recombination.

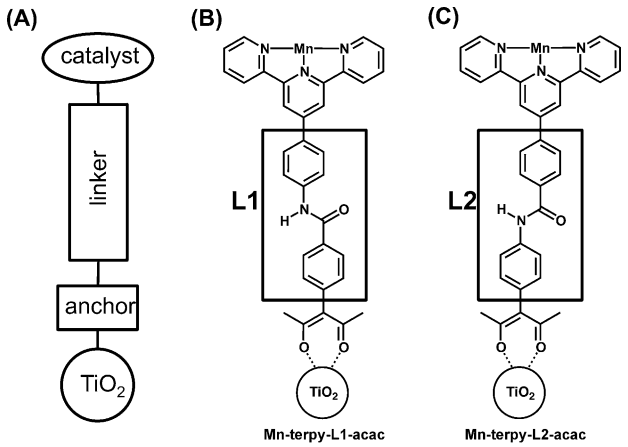

Figure 1. Schematic representation of a functionalized TiO_2 nanoparticle (A), TiO_2 nanoparticle functionalized with **Mn-terpy-L1-acac** (B), and **Mn-terpy-L2-acac** (C). The key difference between L1 and L2 is the direction of the Ph-amide-Ph bridge as indicated with rectangles.

Our findings are supported by calculated current–voltage (*I–V*) curves, based on a combination of density functional theory (DFT) and non-equilibrium Green's function (NEGF) techniques.[30–32] Analysis of these calculated *I–V* curves suggests that rectification in **Mn-terpy-L2-acac** results from the asymmetric shifting of the lowest unoccupied molecular orbital (LUMO) energy level under the influence of negative versus positive bias voltages.[33] We find that the LUMO dominates the overall molecular conductance since it is the state closest to the Fermi level. It is shifted towards (or away from) the Fermi level under negative (or positive) applied voltage bias, favoring reverse versus forward currents. Therefore, we anticipate molecular linkers with similar structural features should also exhibit rectification useful for photocatalysis of multi-electron reactions at metal-oxide surfaces functionalized with transition metal catalysts.

2. Results and Discussion

Our previous work on **Mn-terpy-L1-acac** has demonstrated electron injection and reversible photooxidation of Mn^{II} to Mn^{III} when covalently attached to TiO_2 surfaces.[29,34] The system was specifically designed to include: 1) an acac anchoring group for robust adsorption to semiconductor surfaces, 2) a conjugated light-absorbing unit consisting of two phenyl rings linked by an amide bond, and 3) a terpyridine ligand for binding a metal center such as manganese. We report here an additional terpyridine-acac analog expected to have similar properties.

Specifically, **terpy-L1-acac** was synthesized according to novel synthetic pathways using more efficient coupling reactions and milder conditions than previously reported. The synthesis of **terpy-L2-acac** benefited from the incorporation of well-known terpyridine-phenyl-carboxylic acid (**1**) and was prepared in sufficient purity to produce a crystal for X-ray structural study, a goal not achieved with prior preparative methods (see the Supporting Information). The absorbance spectra of **terpy-L1-acac** and **terpy-L2-acac** on nanoparticulate TiO_2 are shown in Figure 2a. These spectra demonstrate that the optical properties of the two compounds are very similar, consistent with the very small structural difference between the two species. In addition, the THz spectra reported in Figure 2b, show that both systems inject electrons into the TiO_2 conduction band with approximately the same efficiency.

Figure 2b shows the decrease in peak time-domain THz transmission as a function of the delay between the 400 nm pump pulse and the THz probe pulse. The transmission of THz radiation is affected by mobile electrons in the TiO_2 conduction band; therefore, decrease in THz transmission is indicative of an increased electron density in the TiO_2 nanoparticles. When electron injection from two different sensitizers on the same semiconductor material is compared, the magnitude of the change in THz amplitude is a measure of the IET efficiency. Since IET is not strongly influenced by the direction of the amide bond, these results indicate that the photoexcitation–injection pathway originates from the phenyl-acac anchor moiety. That is, upon photoexcitation an electron is transferred on an ultrafast (fs) timescale from the phenyl group through the acac anchor. Electron transfer from Mn^{II} occurs on a much longer timescale and is, therefore, undetectable using this method. Although the THz measurements do not give any direct information about electron transfer through the amide bond, they do confirm that electron injection can occur from both **L1-** and **L2-acac** to TiO_2 and suggest that this initial electron injection is not the determining factor in rectification.

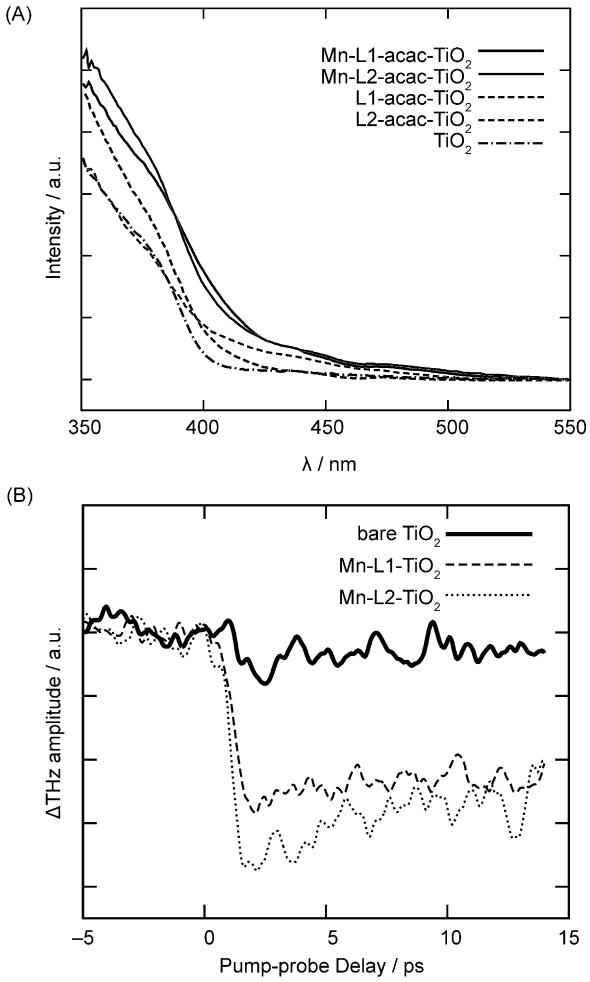

Figure 2. a) Absorbance spectra of TiO_2 nanoparticles functionalized with **terpy-L1-acac** (black) or **terpy-L2-acac** (gray). Coordination of manganese by the terpyridine functionality (solid lines) shifts absorbance to lower wavelengths compared to compounds in the absence of manganese (dashed lines). Spectra were collected on TiO_2 films in diffuse reflectance mode and were normalized at 550 nm to correct for scattering. b) THz spectroscopy for functionalized TiO_2 nanoparticles with **Mn-terpy-L1-acac** (dashed line) and **Mn-terpy-L2-acac** (dotted line) shows that upon photoexcitation both systems undergo electron injection on a sub-ps timescale into TiO_2 nanoparticles.

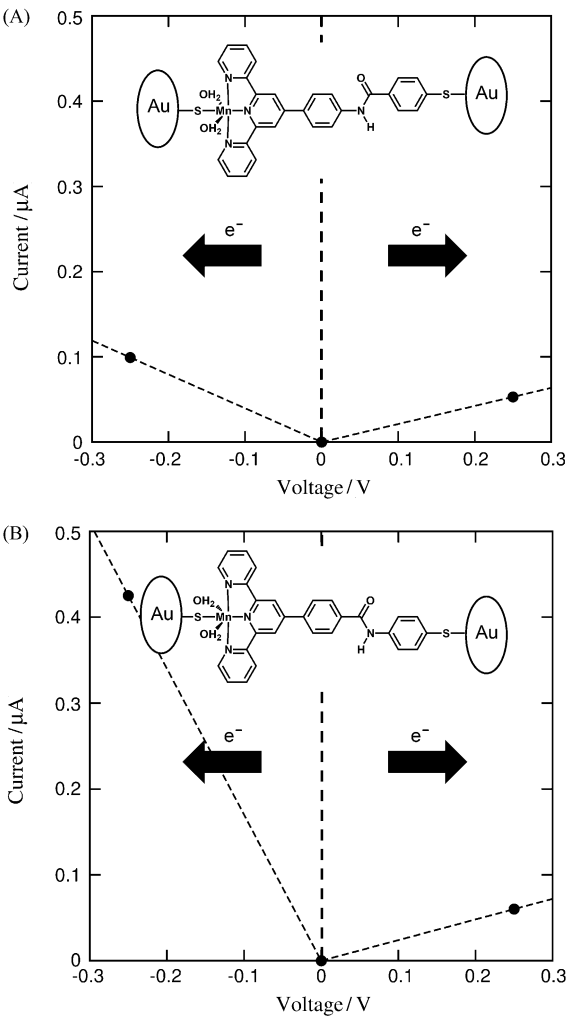

Figure 3. Calculated low bias *I–V* curves for **Mn-terpy-L1** (A) and **Mn-terpy-L2** (B). The vertical dashed line separates the current under positive (right) and negative (left) bias. **Mn-terpy-L2** shows significant rectification while **Mn-terpy-L1** shows only a slight asymmetry.

To compare the electron-transport properties of **L1** and **L2**, the *I–V* characteristics of **Au-Mn-terpy-L1-Au** and **Au-Mn-terpy-L2-Au** junctions were calculated for an applied bias ranging from −0.25 V to 0.25 V. We focus on the range of low bias voltages, most relevant to dye-sensitized solar cells (DSSCs) as determined by the difference between the energy of the photoinjected carrier and the edge of the semiconductor conduction band. Rectification properties at higher bias potentials are beyond the scope of our study since they are not particularly relevant to the energy range of interest for IET in DSSCs. Figure 3 shows that **Mn-terpy-L2** exhibits significant rectification, favoring the reverse current at low bias potentials. In contrast, the I-V curve of **Mn-terpy-L1** has only a slight asymmetry.

As the main difference between **L1** and **L2** is the extent of conjugation due to the direction of the amide bond relative to the terpyridine ligand, we attribute the difference in transport properties to the effect of conjugation and, therefore, electronic delocalization on the level alignment relative to the Fermi level, as discussed below in Figure 6–8. This difference makes the more delocalized LUMO of the **Mn-terpy-L2** molecule closer to the Fermi level and, therefore, more sensitive to the influence of the bias potential. For both **Mn-terpy-L1** and **Mn-terpy-L2**, the positive bias potential shifts the LUMO away from the Fermi level while the negative bias brings the LUMO closer to the Fermi level, favoring the reverse current over the forward current. While this effect is only slightly noticeable in the asymmetry of the I-V curve at low bias potentials for **Mn-terpy-L1**, it is much more pronounced for **Mn-terpy-L2**. These results suggest that both systems could undergo IET to TiO_2 nanoparticles, but **Mn-terpy-L2** will enhance recombination.

To probe the electron transport through the amide linker in the ms timescale, we have measured the change in Mn^{II} signal by using electron paramagnetic resonance (EPR) spectroscopy (Figure 4). For **Mn-terpy-L1-acac**, the EPR signal from Mn^{II} is

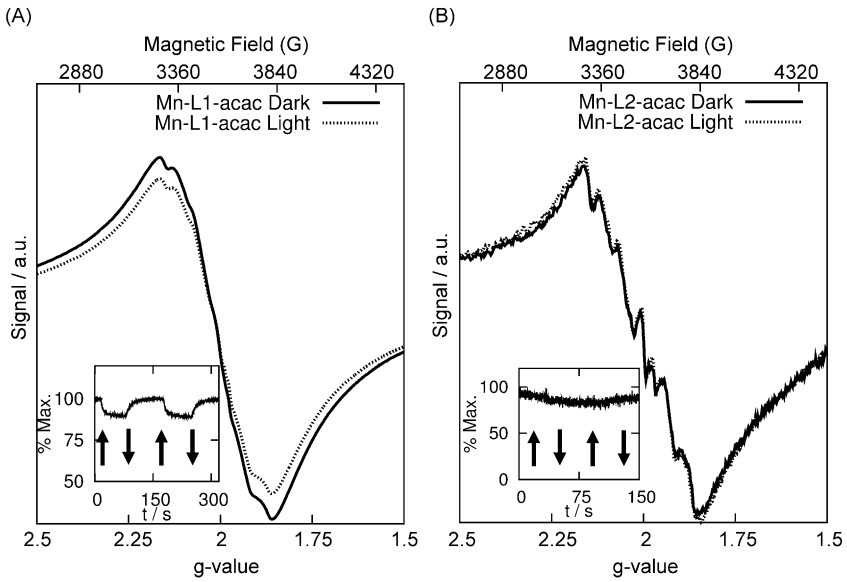

Figure 4. EPR spectroscopy of functionalized TiO_2 nanoparticles with **Mn-terpy-L1-acac** (A) and **Mn-terpy-L2-acac** (B) shows that under steady-state illumination (dotted line) a change in the oxidation state from Mn^{II} to Mn^{III} is detected for **Mn-terpy-L1** and not for **Mn-terpy-L2** in comparison with the signal in the dark (solid line). The insets show time-dependent results for the light-induced change of the Mn^{II} EPR signal measured at the maximum of the first-derivative EPR signal. Arrows denote times when the illumination started (up arrow) and ended (down arrow).

detected before illumination. Upon illumination, Mn^{II} is photooxidized to EPR-silent Mn^{III}, and the signal amplitude decreases (Figure 4a). The signal of Mn^{II} returns to the initial intensity when the lamp is blocked, indicated by up and down arrows in the inset of Figure 4, and in agreement with the previously reported measurements.[29,34] For **Mn-terpy-L2-acac**, the EPR signal from Mn^{II} is detected before illumination, similar to **Mn-terpy-L1-acac**. However, a decrease of the Mn^{II} EPR signal is not detected during steady-state illumination (Figure 4b). In the time-dependent measurement, some baseline drift is observed due to fluctuation in temperature, but the change in amplitude is independent of illumination (Figure 4b, inset). Given that the rate of injection into TiO_2 is shown by terahertz spectroscopy to be very similar for **Mn-terpy-L1-acac** and **Mn-terpy-L2-acac**, the observation of steady-state oxidation of Mn^{II} for **Mn-terpy-L1-acac** suggests that the recombination for **Mn-terpy-L2-acac** is faster than for **Mn-terpy-L1-acac**, consistent with computational predictions of rectification behavior (Figure 3). This indicates that the steady-state light-induced population of Mn^{III} is very small for **Mn-terpy-L2-acac** and, therefore, that recombination processes are faster than Mn^{III} generation processes ($k^b > k^f$).

The observed photochemical properties of **Mn-terpy-L1-acac** may be explained by a simple kinetic model, (Figure 5 and the Supporting Information).[34] In such a kinetic model, the initial IET event is represented by a fast pre-equilibrium between the initial state and the first electron transfer state in which an electron is injected into the TiO_2 conduction band, leaving a hole on the phenyl-acac moiety. This hole may be filled by electron transfer from the terpyridine group through the amide bond in the critical rectification step (k_{12}^f and k_{21}^b). Finally, Mn^{II} is oxidized to Mn^{III} in a third step (k_{23}^f and k_{32}^r). Each step in this model is considered to be reversible, and the contributions from direct charge separation between Mn^{III} and TiO_2 are assumed to be small.

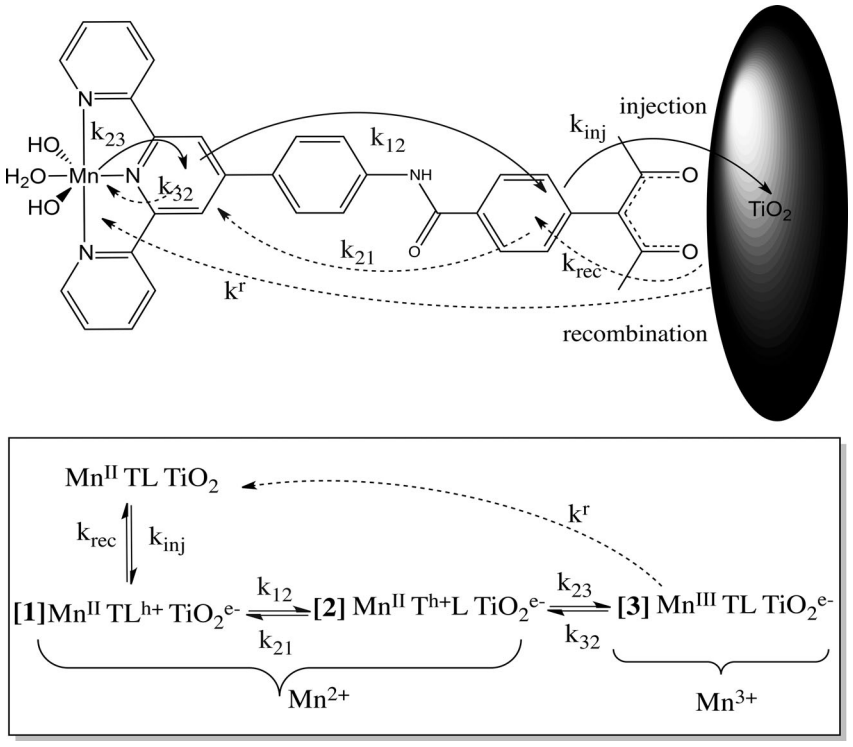

Figure 5. Kinetics of light-induced charge separation for **Mn-terpy-L1-acac** bound to TiO_2 as monitored by EPR. After the initial pre-equilibrium established by ultrafast photoinduced electron injection into TiO_2, the hole is transferred to the terpyridine ligand before oxidizing Mn^{II} to Mn^{III}.

The EPR measurements are performed at 6 K, under low light intensity to avoid changes in temperature that might produce thermal spectral fluctuations. Under these conditions, the time-dependent EPR signal decays by approximately 10% upon photoexcitation of **Mn-terpy-L1-acac**. Under steady-state illumination, the extent of the reaction is dependent on the relative rates for forward and backward electron transfer. In this experiment, $K_1 = k_{12}/k_{21} \approx 5$ (see the Supporting Information), consistent with the observed asymmetry in the calculated *I-V* curve (Figure 3). It is, thus, expected that systems with similar k_{23}/k_{32} and k_{inj}/k_{rec} but with $k_{12} \leq k_{21}$, would show a much smaller decay of the EPR signal as for **Mn-terpy-L2-acac**. A detailed description of the kinetic parameters and estimates for the rate constants based on the EPR data are included in the Supporting Information.

To investigate the origin of rectification at the molecular/electronic level, we compare the local density of states (LDOS) for energy channels close to the Fermi level in **Mn-terpy-L1** and **Mn-terpy-L2** (Figure 6). These channels provide the most significant contributions to the transport properties at low bias voltages, as determined by their contributions to the transmission function in the integration range close to the Fermi level.[35] At the Fermi level, there is no significant electronic density delocalized in the molecular junction between the left and right leads. The closest channel to the Fermi level corresponds to the LUMOs at 180 meV for **Mn-terpy-L2** and 284 meV for **Mn-terpy-L1** above the Fermi level. The LUMO of **Mn-terpy-L2** is more stable and, therefore, closer to the Fermi level since it is more delocalized in the phenyl-terpyridine-amide ligand, as determined by the conjugation of the carbonyl group with the aromatic electronic structure of the phenyl-terpyridine ligand (Figure 7).

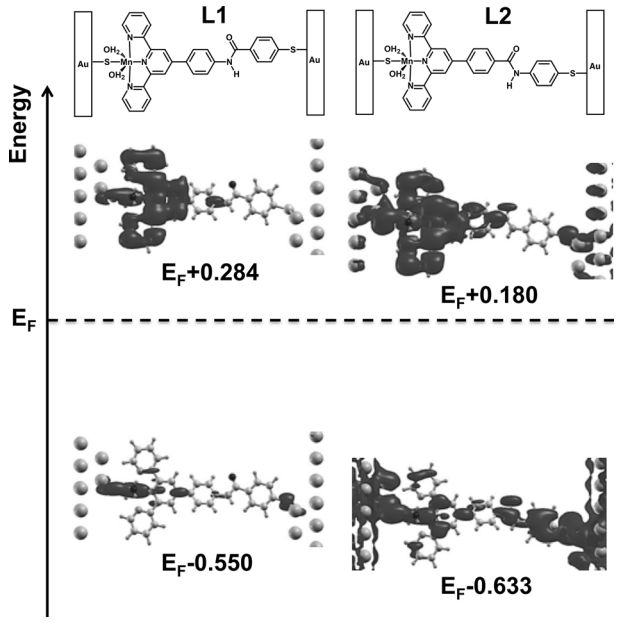

Figure 6. Electronic density for the highest occupied molecular orbital (HOMO) and LUMO states and energies (in eV) for **Mn-terpy-L1** (left) and **Mn-terpy-L2** (right). The contour of electronic density is taken at 1% of its maximum value. For both molecules, the LUMO is the state closest to the Fermi level and provides the most significant contribution to calculated current. While for both molecules, the LUMO is localized on the left half of the junction, for **Mn-terpy-L2**, the electronic density is more delocalized across the entire device region and closer to the Fermi level.

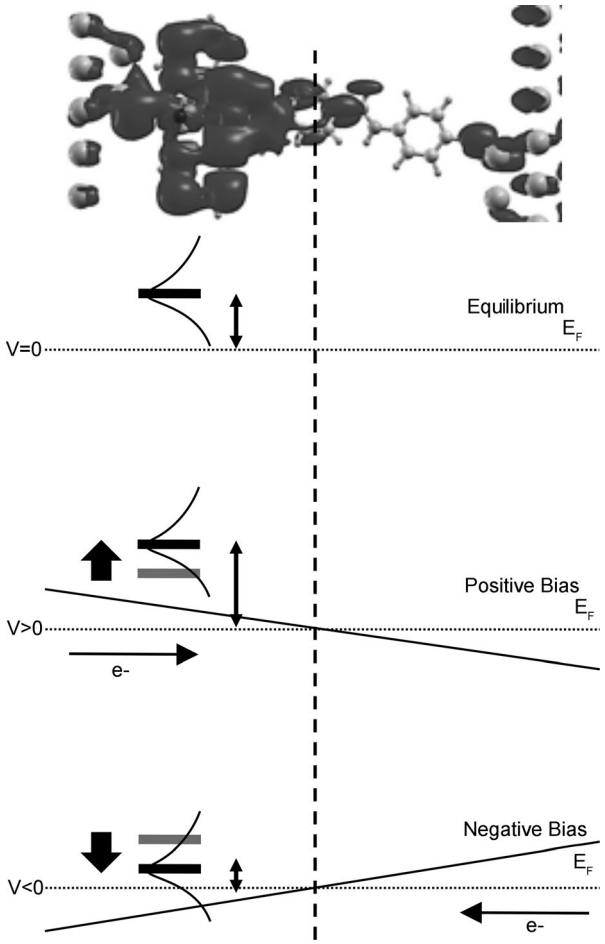

Figure 7. Schematic representation of the LUMO state responsible for electron transport (top) and alignment relative to the Fermi level at equilibrium ($V = 0$, top), positive bias ($V > 0$, middle), and negative bias ($V < 0$, bottom). Due to the localization of the electronic density on the left half of the molecular junction, the LUMO becomes closer to the Fermi level for $V < 0$ while farther away for $V > 0$ (as shown in Figure 8), giving rise to an asymmetric *I–V* curve.

In contrast, the LDOS for **Mn-terpy-L1** is about 100 mV farther away from the Fermi level and more localized on the phenyl-terpyridine region (Figure 6). For both molecules, the LUMO is localized asymmetrically mostly on the Mn-terpyridine half of the molecular junction. Therefore, it approaches the Fermi level under the influence of negative bias potentials that stabilize the phenyl-terpy half of the molecule relative to the phenyl-acac region. Alternately, a positive bias shifts the LUMO farther away from the Fermi level (Figures 7 and 8). Therefore, when comparing **Mn-terpy-L** molecules influenced by low-voltage potentials of the same magnitude but opposite signs (e.g. +250 mV vs. −250 mV), it is clear that the reverse current must be higher that the forward current since the LUMO contribution to the amplitude of the transmission function at the Fermi level is increased by a negative potential and reduced by a positive applied voltage.

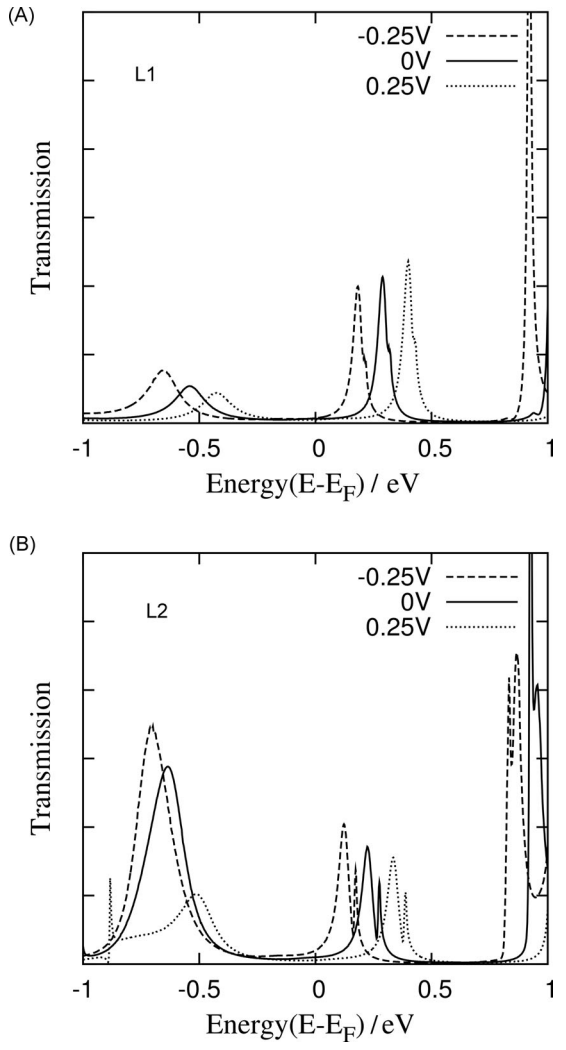

Figure 8. Calculated transmission functions for A) **Mn-terpy-L1** and B) **Mn-terpy-L2** at zero bias ($V=0$, black), positive bias ($V=250$ mV, dotted line), and negative bias ($V=-250$ mV, dashed line). For both systems, the LUMO dominates the overall conductance since it is the closest state to the Fermi level. Due to the LUMO asymmetry in charge distribution, the LUMO state becomes closer to the Fermi level for $V<0$ and farther away for $V>0$, giving rise to the asymmetric *I–V* characteristic curve.

We note that the rectification mechanism observed at low bias potentials is determined by a single state (i.e. the LUMO) that dominates the electron transport across the molecular junction. Therefore, the rectification process is quite different from mechanisms based on donor-acceptor dyads where donor and acceptor states in the molecule participate in the transport mechanism, as originally proposed by Ratner and co-workers.[20]

These results show that a suitable choice in the orientation of a single amide bond can enhance or suppress rectification, even for molecular linkers where forward and reverse charge transport is dominated by a single channel. Therefore, as shown by various groups,[35–37] we observe that small structural changes can produce remarkable differences in the molecular transport properties.

3. Conclusions

We have reported the synthesis, spectroscopy, and electron-transport calculations characterizing two molecular assemblies relevant to solar-energy technology that provide fundamental insight on the molecular origin of current rectification. Our results show that assemblies based on **Mn-terpy-L1** and **Mn-terpy-L2** induce photoconversion by IET. Remarkably, the directional orientation of a single amide bond leads to dramatic differences in the transport properties of the two assemblies. While **Mn-terpy-L1** is characterized by a nearly symmetric I-V curve, **Mn-terpy-L2** exhibits significant rectification, thereby preventing photooxidation of the Mn center by favoring reverse current over forward electron transport. Our findings are supported by NEGF-DFT calculations and measurements of electron transfer processes probed by THz and EPR spectroscopies.

We have found that the underlying rectification mechanism, observed for **Mn-terpy-L2** at low bias voltages, can be traced to the distinct response of the LUMO towards positive and negative potentials. Contrary to mechanisms based on donor–acceptor dyads where donor and acceptor states in the molecule participate in the transport mechanism, rectification in **Mn-terpy-L2** is determined by the asymmetric distribution of charge in the LUMO giving the resulting stabilization (or destabilization) relative to the Fermi level, as influenced by negative (or positive) potentials. The elucidated rectification mechanism thus complements other possible rectification processes, including schemes based on donor-acceptor dyads,[20] and rectification based on controlled molecular orientation as reported by Tao and co-workers.[38]

The comparative analysis of **Mn-terpy-L1** and **Mn-terpy-L2** shows that the extent of conjugation is critical to level alignment and, therefore, can be exploited in the design of molecular linkers with suitable rectification properties. Ongoing work is exploring the application of this concept to the design of TiO_2 photoanodes functionalized with oxo-manganese adsorbates and porphyrin dyes for light-driven water oxidation.[34,39]

Experimental Section

Synthesis

Syntheses were performed using standard Schlenk techniques under N_2 atmosphere unless otherwise noted. Proton and carbon NMR spectra were obtained using Bruker spectrometers operating at 400 and 500 MHz, respectively. Chemical shifts are reported in ppm (δ) with residual solvent used as the internal reference. 4-(4′phenyl-2,2′:6′,2″-terpyridyl)benzoic acid[40] (**1**), 3-(4-nitrophenyl)-1-(pyridin-2-yl)prop-2-en-1-one[41] (**2**), and 4-(2-hydroxy-4-oxopent-2-en-3-yl)benzoic acid[42] (**3**) were synthesized according to literature procedures. Copper(I) iodide was purified using potassium iodide and activated carbon.[43] Dichloromethane and tetrahydrofuran were dried with a solvent purification system using a 1 m column containing activated alumina. All other reagents and solvents were commercially available and used as received.

The synthesis of 2-acetylpyridine pyridinium iodide (**4**) (Scheme 1) was carried out according to published procedures.[44] Minor modi-

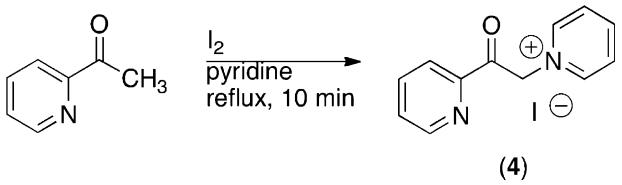

Scheme 1. Synthesis of 2-acetylpyridinium iodide (**4**).

fications were performed as follows: 2-acetylpyridine (24.76 mmol, 3.0 g, 2.83 mL) and freshly sublimed iodine (24.76 mmol, 6.28 g) were dissolved in 12.0 mL of pyridine and refluxed under N_2 for 10 min. The solvent was then removed in vacuum and the resulting black solid was purified by silica flash column chromatography using acetonitrile as an eluent. The crude product was obtained as a cream-colored solid which was recrystallized from hot ethanol to give 4.312 g (54% yield) of **4** as a tan crystalline solid. ^{1}H NMR (400 MHz, CD_3CN) δ = 8.88–8.77 (m, 1H), 8.77–8.70 (m, 2H), 8.71–8.59 (m, 1H), 8.14 (t, J = 7.1 Hz, 2H), 8.07 (ddd, J = 8.8, 4.5, 1.3 Hz, 2H), 7.74 (ddd, J = 7.1, 4.8, 1.7 Hz, 1H), 6.41 ppm (s, 2H).

Nitrophenyl-terpyridine **5** (Scheme 2) was synthesized according to a published procedure[45] with minor modifications. Pyridinium iodide (**4**) (6.72 mmol, 2.193 g), 3-(4-nitrophenyl)-1-(pyridin-2-yl)prop-2-en-1-one (**2**) (6.72 mmol, 1.708 g), and dry ammonium

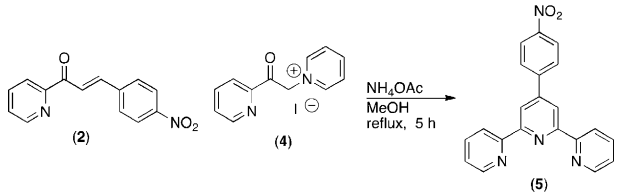

Scheme 2. Synthesis of nitrophenyl-terpyridine (**5**).

acetate (6.0 equiv, 40.3 mmol, 3.11 g) were dissolved in methanol (100 mL) and refluxed for 5 h during which time a white solid precipitated. The solid was collected by vacuum filtration and washed with cold methanol to give 1.93 g (81% yield) of **5** as a white solid. ^{1}H NMR (400 MHz, $CDCl_3$) δ = 8.75 (s, 2H), 8.75–8.72 (m, 2H), 8.69 (d, J = 8.0 Hz, 2H), 8.37 (d, J = 8.8 Hz, 2H), 8.05 (d, J = 8.8 Hz, 2H), 7.91 (td, J = 7.7, 1.8 Hz, 2H), 7.39 ppm (ddd, J = 7.4, 4.8, 1.1 Hz, 2H).[40]

Amino-phenyl-terpyridine **6** (Scheme 3) was synthesized according to the literature procedure[46] from **5** using hydrazine hydrate (55% soln.) and palladium on carbon in refluxing ethanol to give a white solid. The ^{1}H NMR spectrum matches previously reported data. ^{1}H NMR (400 MHz, $CDCl_3$) δ = 8.74–8.71 (m, 1H), 8.69 (s, 1H), 8.66 (dd, J = 8.0, 0.8 Hz, 1H), 7.87 (td, J = 7.7, 1.8 Hz, 1H), 7.82–7.75 (m,

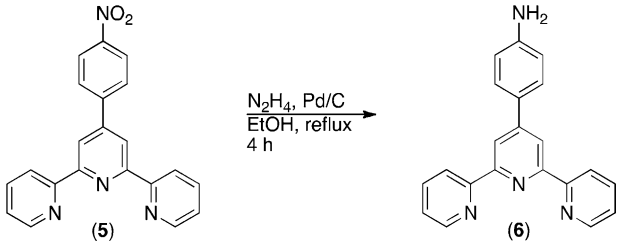

Scheme 3. Synthesis of aminophenyl-terpyridine (**6**).

1H), 7.34 (ddd, J = 7.5, 4.8, 1.2 Hz, 1H), 6.83–6.77 (m, 1H), 3.87 (s, 1H).

Although **terpy-L1-acac** has been previously synthesized,[29] a new route is reported below (Scheme 4). 4-(2-hydroxy-4-oxopent-2-en-3-yl)benzoic acid (**3**) (500 mg, 2.272 mmol, 1.5 eq), 1-ethyl-3-[3-dimethylaminopropyl] carbodiimide hydrochloride (EDC-HCl, 508 mg,

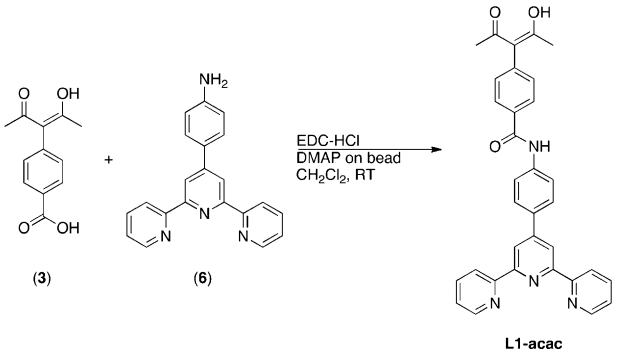

Scheme 4. Synthesis of **terpy-L1-acac**.

2.65 mmol, 1.75 equiv), 4-dimethylaminopyridine on polystyrene beads (loading 3.0 mmol DMAP/g, 1.77 g, 5.3 mmol, 3.5 equiv), and dry dichloromethane (DCM, 3 mL) were loaded into a 100 mL round bottom flask wrapped in aluminum foil and placed under N_2 atmosphere. A separate flask was loaded with 4-([2,2′:6′,2″-terpyridin]-4′-yl)aniline (**6**) (491 mg, 1.515 mmol, 1.0 eq) and dry DCM (10 mL), placed under N_2, and cannulated into the first flask. After stirring at room temperature for 20 h, the mixture was diluted with DCM, filtered to remove the polystyrene beads, and transferred to a separatory funnel. The organic layer was washed with distilled water and brine, dried over sodium sulfate, and then concentrated in vacuum to give a cream-colored solid in 50% yield. ^{1}H NMR (500 MHz, $CDCl_3$) δ = 16.72 (s, 1H), 8.77–8.73 (m, 4H), 8.68 (d, J = 8.0 Hz, 2H), 8.04 (s, 1H), 7.95 (dd, J = 9.8, 8.5 Hz, 4H), 7.89 (td, J = 7.7, 1.8 Hz, 2H), 7.83 (d, J = 8.6 Hz, 2H), 7.41–7.31 (m, 4H), 1.91 (s, 6H). Crystals suitable for X-ray analysis were grown by slow evaporation of benzene (see the Supporting Information).

The synthesis of **8** (Scheme 5) was carried out in an analogous manner to the preparation used by Jiang et al.[42] to synthesize 3-(3-nitrophenyl)pentane-2,4-dione. A mixture of 1-iodo-4-nitroben-

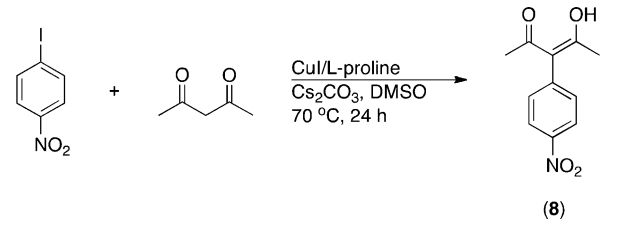

Scheme 5. Synthesis of nitrophenyl-acac (**8**).

zene (2.0 mmol), 2,4-pentanedione (6.0 mmol), cesium carbonate (8.0 mmol), freshly recrystallized copper(I) iodide (0.20 mmol), and L-proline (0.40 mmol) in dry dimethylsulfoxide (DMSO, 10 mL) was charged in a flask wrapped in aluminum foil to protect from light and heated at 70 °C under nitrogen atmosphere for 24 h.

The cooled solution was poured into 1 M HCl and extracted with ethyl acetate. The organic layer was washed with brine, dried over

Na_2SO_4, and the solvent removed in vacuum. The crude residue was purified on a flash silica gel column using a mixture of hexanes:ethyl acetate (7:3) as eluent to afford 292 mg (64% yield) of **8** as a yellow solid. The product was then recrystallized with hexanes to give a slightly yellow crystalline solid. ^{1}H NMR (400 MHz, $CDCl_3$) $\delta =$ 16.78 (s, 1H), 8.27 (dd, $J = 2.1$, 8.9, 2H), 7.39 (dd, $J = 2.1$, 8.9, 2H), 1.90 (s, 6H). ^{13}C NMR ($CDCl_3$, 500 MHz): $\delta = 190.5$, 147.3, 144.0, 132.1, 124.0, 113.6, 24.2. HRMS calcd (found) for $C_{11}H_{11}NO_4$ M+: 222.076084 (222.07611).

A mixture of **8** (3.14 mmol) and Pd/C (10 wt.%, 104 mg) was stirred in a 1:1 DCM:ethanol mixture (40 mL) and degassed thoroughly with N_2 at room temperature for 20 min (Scheme 6). Hydrogen gas

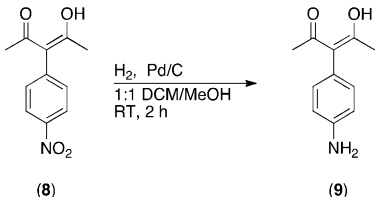

Scheme 6. Synthesis of aminophenyl-acac (**9**).

(H_2) was then bubbled into the reaction vessel using a balloon and was allowed to stir under H_2 atmosphere for 2 h. The resulting solution was then purged with N_2, filtered through Celite, and washed with ethanol and DCM. The solvent was then removed in vacuo and the crude product was purified on a silica gel column (80:20 hexanes : ethyl acetate) and recrystallized in hexanes to give off-white needles to yield 420 mg (2.20 mmol, 70% yield) of **9**. ^{1}H NMR (500 MHz, $CDCl_3$) $\delta = 16.61$ (s, 1H), 6.93 (d, $J = 8.5$ Hz, 2H), 6.71 (d, $J = 8.5$ Hz, 2H), 1.89 (s, 6H). ^{13}C NMR ($CDCl_3$, 500 MHz): $\delta =$ 190.3, 144.6, 130.9, 125.9, 125.7, 114.2, 23.1. ESI molecular ion calculated for $C_{11}H_{11}NO_4H^+$: 192.10, found: 192.04.

Terpy phenyl acid (**1**) (100 mg, 0.28 mmol) and thionyl chloride ($SOCl_2$, 10.0 eq, 3.5 mmol, 0.25 mL) were refluxed under nitrogen in DCM (10 mL) for 2 h (Scheme 7). The remaining $SOCl_2$ was removed by short-path distillation and dried for 2 h. DCM (10 mL), *N*,*N*-diisopropylethylamine (3.0 equiv, 0.75 mmol, 0.13 mL) and a solution of **9** (1.1 eq) in 4 mL of DCM were added to the flask and the mixture was refluxed under N_2 for 16 h. The resulting mixture was evaporated in vacuum and purified by flash column chromatography on silica gel.

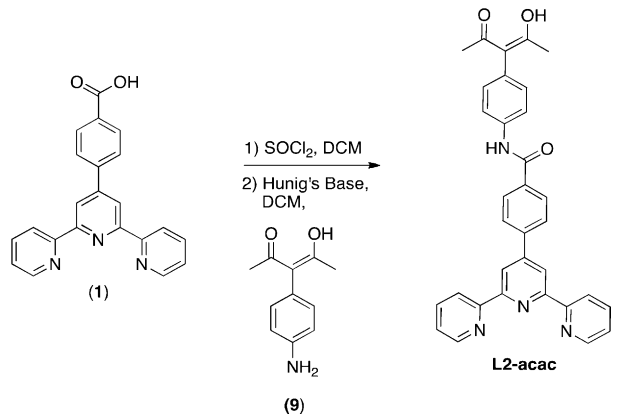

Scheme 7. Synthesis of **terpy-L2-acac.**

Gradient elution with 20% to 100% ethyl acetate in hexanes afforded **terpy-L2-acac** (50 mg, 0.10 mmol, 40% yield) as colorless crystals suitable for X-ray analysis (see the Supporting Information). $C_{33}H_{26}N_4O_3 \cdot H_2O$ (calc: C 75.27; H: 4.98; N: 14.70; found: C 72.78; H 3.76; N 14.78) ^{1}H NMR (400 MHz, [D_6]DMSO) $\delta = 16.82$ (s, 1H), 10.50 (s, 1H), 8.79 (d, $J = 2.5$, 4H), 8.72 (d, $J = 7.9$, 2H), 8.16 (dd, $J = 8.5$, 26.8, 4H), 8.08 (td, $J = 1.7$, 7.8, 2H), 7.91–7.85 (m, 2H), 7.63–7.52 (m, 2H), 7.33–7.23 (m, 2H), 1.90 (s, 6H). ^{13}C NMR (500 MHz, [D_6]DMSO) $\delta = 190.83$, 165.01, 155.77, 154.77, 149.32, 148.45, 140.28, 138.23, 137.25, 135.44, 131.51, 131.24, 128.72, 126.98, 124.58, 120.95, 120.44, 118.06, 114.40, 23.90 ppm.

TiO_2 Functionalization with Mn-terpy-L-Acac

The samples for time-resolved EPR studies were prepared by stirring Degussa P25 TiO_2 nanoparticles (30 mg) with complex **terpy-L1-acac** or **terpy-L2-acac** (3.0 mg, 0.0056 mmol) in dry DCM (2 mL) at reflux for 2 h. The suspension was cooled and filtered, and the light yellow solid was washed with DCM (10 mL) and vacuum-dried. The powder was then transferred to a 5 mL round-bottom flask containing $Mn(OAc)_2$tetrahydrate (5 mg) and water (3 mL). The suspension was stirred at room temperature for 12 h, filtered, washed with excess water, and vacuum-dried. The powdered samples were then loaded into melting-point capillary tubes; mass and sample heights were then measured to verify sample-to-sample uniformity. The capillary tube was then flame-sealed before being loaded into an EPR tube.

EPR Spectroscopy

Perpendicular-mode EPR data were collected on an X-band Bruker Biospin/ELEXSYS E500 spectrometer equipped with an SHQ cavity and an Oxford ESR-900 liquid helium cryostat. All spectra were collected at 7 K on powered samples sealed in capillary tubes placed in 5 mm o.d. (outside diameter) quartz EPR tubes containing 60/40 (V/V) toluene/acetone. This solvent mixture forms a transparent glass for efficient illumination of the sample and allows efficient heat transfer to prevent heating of the sample during illumination. Samples were illuminated in the cryostat at 7 K with white light from a Fiber-Lite Series 180 illuminator (Dolan–Jennings Industries, Inc.) passed through 425 nm long-pass and water filters. Spectra were recorded with the following settings: modulation amplitude = 10 G, modulation frequency = 100 kHz, microwave power = 0.05 mW, and microwave frequency = 9.357 GHz.

Time-Resolved Terahertz Spectroscopy

The samples for time-resolved terahertz spectroscopy consist of thin mesoporous films (~20 microns) of Degussa P25 TiO_2 nanoparticles. The nanoparticles were doctor bladed from aqueous solution onto a glass cover slip and annealed at 360 °C for 30 min. Degussa P25 consists of 25 nm particles that are 70% anatase and 30% rutile. The TiO_2 thin films are sensitized by soaking them overnight in 2 mM solution of either **terpy-L1-acac** or **terpy-L2-acac** in dichloromethane and then rinsing the slide with copious amounts of dichloromethane. An amplified Ti:Sapphire laser (Tsunami/Spitfire from Spectra Physics) generated 800 mW of pulsed near-IR light at a 1 kHz repetition rate. The pulse width was 150 fs, and the center wavelength was 800 nm. Approximately two-thirds of the power was frequency doubled to produce 40 mW of 400 nm (3.10 eV) light for the pump beam. The remainder of the near-IR light was used to generate THz radiation using optical rectification in a ZnTe(110) crystal and detect it via free space electron-optic sampling in an additional ZnTe(110) crystal. Terahertz data were taken

at room temperature, and the average of two samples was taken for each data set. More details about the THz spectroscopy apparatus can be found in previously published reports.[29,47,48]

Theoretical and Computational Methods

Geometries were optimized at the DFT B3LYP level using a combination of basis sets (6-31G(d,p) for non-metal elements and LANL2DZ for Mn atom) as implemented in Gaussian 09.[49] Current–voltage characteristic curves were obtained by using the NEGF-DFT approaches implemented in the TranSIESTA computational package.[50] The molecular models were designed in the usual three-system model (extended molecule), including the left electrode lead, central device region, and right electrode lead. The transport properties were calculated using an electronic structure calculation for the leads treating them as semi-infinite periodic nanowires which were later connected to the scattering (central) region. The coordinates for the extended molecules as well as sample input files for transport calculations used in this work are provided in the Supporting Information.

The electrode leads were modeled based on the Au(1,1,1) crystal lattice. The molecules were connected to the gold electrodes via thiol anchoring groups. A polarized single- ζ basis set was used for gold atoms and polarized double-ζ basis set[51] for all non-gold atoms in all transport calculations, which is sufficient to describe the dominant energy levels involved in electron transport. For exchange correlation functional, we used the generalized gradient approximation[52] (GGA). To sample the Brillouin zone, we used a 10×10×80 Monkhorst k-grids[53,54] for the leads and 10×10×1 Monkhorst type k-grid for the device region. The energy cutoff for the real space grid was 250 Ry (Rydberg).

From the DFT density ρ, one can obtain the Hamiltonian and overlap matrices [Eq. (2)]:

$$H_{JK}^{\alpha\beta} = \left\langle \psi_J^{\alpha\beta} \middle| H(\rho) \middle| \psi_K^{\alpha\beta} \right\rangle \tag{2}$$

and [Eq. (3)]:

$$S_{JK}^{\alpha\beta} = \left\langle \psi_J^{\alpha\beta} \middle| \psi_K^{\alpha\beta} \right\rangle \tag{3}$$

where J and K are either L, R or M, labeling the left lead, right lead or the molecule, respectively; and α and β represent orbitals inside the respective regions.
This information is used to obtain the Green's function of the molecule [Eq. (4)]:

$$G_M = \frac{1}{\varepsilon S - H - \Sigma_L - \Sigma_R} \tag{4}$$

where ε is the energy plus an infinitesimal positive imaginary part ($E + i\delta$), and the $\Sigma_{L/R}$ functions are the self-energy terms of the left and right leads.
The electron density ρ is defined as [Eq. (5)]:

$$\frac{1}{2\pi}\int G_M^<(E)\mathrm{d}E \tag{5}$$

The lesser Green's function has the expression [Eq. (6)]:

$$G_M^<(E) = iG_M^+(E)\left[\Gamma_L f(E-\mu_L) + \Gamma_R(E-\mu_R)G_M^-(E)\right] \tag{6}$$

where [Eq. (7)]:

$$\Gamma_{L/R} = i\left(\Sigma_{L/R}^+ - \Sigma_{L/R}^-\right) \tag{7}$$

and f is the Fermi distribution function based on the shifting of chemical potential of the electrodes according to finite bias V in the non-equilibrium regime [Eq. (8)]:

$$\mu_{L/R} = E_F \pm V/2 \tag{8}$$

Self-consistency calculations are performed for the electron density until convergence is achieved. The transmission coefficient is obtained with the Fisher–Lee formula [Eq. (9)]:

$$T = Tr\left[\Gamma_L G_M^- \Gamma_R G_M^+\right] \tag{9}$$

while the current is obtained by integrating the transmission [Eq. (10)]:

$$I = \frac{2e}{h}\int T(E)[f(E-\mu_L) - f(E-\mu_R)]\mathrm{d}E \tag{10}$$

To interpret the calculated current–voltage curves, we recalculated the LDOS, that is, the electronic density distribution for the state with energy ε_k, based on the electronic structure of each extended system. The LDOS distributions were obtained by integrating the Green's function in real space [Eq. (11)]:

$$n(r) = \frac{1}{\pi}\int_{\varepsilon_k-\delta}^{\varepsilon_k+\delta} \mathrm{Im}[G(r,\varepsilon)]\mathrm{d}\varepsilon \tag{11}$$

where ε_k is the energy of the state of interest and δ is chosen to cover the width of that state.

Acknowledgements

We acknowledge support for the spectroscopic work by the U.S. Department of Energy Grant DE-FG02-07ER15909 (G.W.B. and C.A.S) and for the synthetic work by DE-PS02-08ER15944 (R.H.C). Computational work was supported as part of the Argonne-Northwestern Solar Energy Research (ANSER) Center, an Energy Frontier Research Center funded by the U.S. Department of Energy, Office of Science, Office of Basic Energy Sciences under Award Number DE-SC0001059 (V.S.B). Computer resources were provided by NERSC and by the High performance Computing facilities at Yale University. Philip Coppens and Jiji Tang (SUNY Buffalo) and Nathan D. Schley (Yale University) are gratefully acknowledged for solving the crystal structures of ***terpy-L1-acac*** *and* ***terpy-L2-acac****, respectively.*

Keywords: density functional theory · dye-sensitized solar cells · electron transport · molecular rectifier · photocatalysis

[1] V. Balzani, A. Credi, M. Venturi, *ChemSusChem* **2008**, *1*, 26 – 58.
[2] I. McConnell, G. H. Li, G. W. Brudvig, *Chem. Biol.* **2010**, *17*, 434 – 447.
[3] C. W. Cady, R. H. Crabtree, G. W. Brudvig, *Coord. Chem. Rev.* **2008**, *252*, 444 – 455.
[4] E. M. Sproviero, J. A. Gascon, J. P. McEvoy, G. W. Brudvig, V. S. Batista, *Curr. Opin. Struct. Biol.* **2007**, *17*, 173 – 180.

[5] E. M. Sproviero, J. A. Gascon, J. P. McEvoy, G. W. Brudvig, V. S. Batista, *Coord. Chem. Rev.* **2008**, *252*, 395 – 415.
[6] G. H. Li, E. M. Sproviero, W. R. McNamara, R. C. Snoeberger, R. H. Crabtree, G. W. Brudvig, V. S. Batista, *J. Phys. Chem. B* **2010**, *114*, 14214 – 14222.
[7] G. F. Moore, S. J. Konezny, H. E. Song, R. L. Milot, J. D. Blakemore, M. L. Lee, V. S. Batista, C. A. Schmuttenmaer, R. H. Crabtree, G. W. Brudvig, *J. Phys. Chem. C* **2012**, *116*, 4892 – 4902.
[8] D. Q. Xiao, L. A. Martini, R. C. Snoeberger, R. H. Crabtree, V. S. Batista, *J. Am. Chem. Soc.* **2011**, *133*, 9014 – 9022.
[9] G. H. Li, E. M. Sproviero, R. C. Snoeberger, N. Iguchi, J. D. Blakemore, R. H. Crabtree, G. W. Brudvig, V. S. Batista, *Energy Environ. Sci.* **2009**, *2*, 230 – 238.
[10] W. R. McNamara, R. L. Milot, H. E. Song, R. C. Snoeberger, V. S. Batista, C. A. Schmuttenmaer, G. W. Brudvig, R. H. Crabtree, *Energy Environ. Sci.* **2010**, *3*, 917 – 923.
[11] W. R. McNamara, R. C. Snoeberger, G. Li, J. M. Schleicher, C. W. Cady, M. Poyatos, C. A. Schmuttenmaer, R. H. Crabtree, G. W. Brudvig, V. S. Batista, *J. Am. Chem. Soc.* **2008**, *130*, 14329 – 14338.
[12] W. R. McNamara, R. C. Snoeberger, G. H. Li, C. Richter, L. J. Allen, R. L. Milot, C. A. Schmuttenmaer, R. H. Crabtree, G. W. Brudvig, V. S. Batista, *Energy Environ. Sci.* **2009**, *2*, 1173 – 1175.
[13] K. Rajeshwar, *J. Appl. Electrochem.* **2007**, *37*, 765 – 787.
[14] A. L. Linsebigler, G. Q. Lu, J. T. Yates, *Chem. Rev.* **1995**, *95*, 735 – 758.
[15] O. Carp, C. L. Huisman, A. Reller, *Prog. Solid State Chem.* **2004**, *32*, 33 – 177.
[16] Y. C. Nah, I. Paramasivam, P. Schmuki, *ChemPhysChem* **2010**, *11*, 2698 – 2713.
[17] X. T. Hong, Z. P. Luo, J. D. Batteas, *J. Solid State Chem.* **2011**, *184*, 2244 – 2249.
[18] T. W. Hamann, R. A. Jensen, A. B. F. Martinson, H. Van Ryswyk, J. T. Hupp, *Energy Environ. Sci.* **2008**, *1*, 66 – 78.
[19] G. H. Li, C. P. Richter, R. L. Milot, L. Cai, C. A. Schmuttenmaer, R. H. Crabtree, G. W. Brudvig, V. S. Batista, *Dalton Trans.* **2009**, 10078 – 10085.
[20] A. Aviram, M. A. Ratner, *Chem. Phys. Lett.* **1974**, *29*, 277 – 283.
[21] R. M. Metzger, *Chem. Phys.* **2006**, *326*, 176 – 187.
[22] R. M. Metzger, *J. Mater. Chem.* **2008**, *18*, 4364 – 4396.
[23] W. A. Reinerth, L. Jones, T. P. Burgin, C. W. Zhou, C. J. Muller, M. R. Deshpande, M. A. Reed, J. M. Tour, *Nanotechnology* **1998**, *9*, 246 – 250.
[24] J. Chen, M. A. Reed, A. M. Rawlett, J. M. Tour, *Science* **1999**, *286*, 1550 – 1552.
[25] J. Chen, M. A. Reed, *Chem. Phys.* **2002**, *281*, 127 – 145.
[26] M. Petty, M. R. Bryce, D. Bloor, *An Introduction to Molecular Electronics*, Oxford University Press, New York, **1995**.
[27] L. A. Bumm, J. J. Arnold, M. T. Cygan, T. D. Dunbar, T. P. Burgin, L. Jones, D. L. Allara, J. M. Tour, P. S. Weiss, *Science* **1996**, *271*, 1705 – 1707.
[28] J. He, O. Sankey, M. Lee, N. J. Tao, X. L. Li, S. Lindsay, *Faraday Discuss.* **2006**, *131*, 145 – 154.
[29] W. R. McNamara, R. C. Snoeberger, G. Li, J. M. Schleicher, C. W. Cady, M. Poyatos, C. A. Schmuttenmaer, R. H. Crabtree, G. W. Brudvig, V. S. Batista, *J. Am. Chem. Soc.* **2008**, *130*, 14329 – 14338.
[30] L. V. Keldysh, *Soviet Physics Jetp-USSR* **1965**, *20*, 1018 – 1026.
[31] S. Datta in *Electronic Transport in Mesoscopic Systems*, Cambridge University Press, Cambridge, **1997**.
[32] S. Datta, *Quantum Transport*, Cambridge University Press, Cambridge, **2005**.
[33] Y. Tsuji, K. Yoshizawa, *J. Phys. Chem. C* **2012**, *116*, 26625 – 26635.
[34] A. C. Durrell, G. Li, M. Koepf, K. J. Young, C. F. A. Negre, L. J. Allen, W. R. McNamara, H.-e. Song, V. S. Batista, R. H. Crabtree, G. W. Brudvig, *J. Catal.* **2014**, *310*, 37 – 44.
[35] J. L. Palma, C. Cao, X. G. Zhang, P. S. Krstic, J. L. Krause, H. P. Cheng, *J. Phys. Chem. C* **2010**, *114*, 1655 – 1662.
[36] J. Huang, Q. Li, H. Ren, H. Su, Q. W. Shi, J. Yang, *J. Chem. Phys.* **2007**, *127*, 094705.
[37] X. Y. Xiao, B. Q. Xu, N. J. Tao, *Nano Lett.* **2004**, *4*, 267 – 271.
[38] I. Diez-Perez, J. Hihath, Y. Lee, L. P. Yu, L. Adamska, M. A. Kozhushner, I. I. Oleynik, N. J. Tao, *Nat. Chem.* **2009**, *1*, 635 – 641.
[39] C. F. A. Negre, R. L. Milot, L. A. Martini, W. Ding, R. H. Crabtree, C. A. Schmuttenmaer, V. S. Batista, *J. Phys. Chem. C* **2013**, *117*, 24462 – 24470.
[40] E. C. Constable, E. L. Dunphy, C. E. Housecroft, M. Neuburger, S. Schaffner, F. Schaper, S. R. Batten, *Dalton Trans.* **2007**, 4323 – 4332.
[41] G. A. Koohmareh, M. Sharifi, *J. Appl. Polym. Sci.* **2010**, *116*, 179 – 183.
[42] Y. W. Jiang, N. Wu, H. H. Wu, M. Y. He, *Synlett* **2005**, 2731 – 2734.
[43] G. B. Kauffman, L. Y. Fang, *Inorg. Synth.* **1983**, *22*, 101 – 103.
[44] S. H. Wadman, J. M. Kroon, K. Bakker, R. W. A. Havenith, G. P. M. van Klink, G. van Koten, *Organometallics* **2010**, *29*, 1569 – 1579.
[45] S. Bonnet, J.-P. Collin, J.-P. Sauvage, *Inorg. Chem.* **2007**, *46*, 10520 – 10533.
[46] P. Laine, F. Bedioui, P. Ochsenbein, V. Marvaud, M. Bonin, E. Amouyal, *J. Am. Chem. Soc.* **2002**, *124*, 1364 – 1377.
[47] M. C. Beard, G. M. Turner, C. A. Schmuttenmaer, *Phys. Rev. B* **2000**, *62*, 15764 – 15777.
[48] J. B. Baxter, C. A. Schmuttenmaer, *J. Phys. Chem. B* **2006**, *110*, 25229 – 25239.
[49] *Gaussian 09 (Revision A.1)*, M. J. Frisch, G. W. Trucks, H. B. Schlegel, G. E. Scuseria, M. A. Robb, J. R. Cheeseman, G. Scalmani, V. Barone, B. Mennucci, G. A. Petersson, H. Nakatsuji, M. Caricato, X. Li, H. P. Hratchian, A. F. Izmaylov, J. Bloino, G. Zheng, J. L. Sonnenberg, M. Hada, M. Ehara, K. Toyota, R. Fukuda, J. Hasegawa, M. Ishida, T. Nakajima, Y. Honda, O. Kitao, H. Nakai, T. Vreven, J. A. Montgomery, Jr., J. E. Peralta, F. Ogliaro, M. Bearpark, J. J. Heyd, E. Brothers, K. N. Kudin, V. N. Staroverov, R. Kobayashi, J. Normand, K. Raghavachari, A. Rendell, J. C. Burant, S. S. Iyengar, J. Tomasi, M. Cossi, N. Rega, N. J. Millam, M. Klene, J. E. Knox, J. B. Cross, V. Bakken, C. Adamo, J. Jaramillo, R. Gomperts, R. E. Stratmann, O. Yazyev, A. J. Austin, R. Cammi, C. Pomelli, J. W. Ochterski, R. L. Martin, K. Morokuma, V. G. Zakrzewski, G. A. Voth, P. Salvador, J. J. Dannenberg, S. Dapprich, A. D. Daniels, Ö. Farkas, J. B. Foresman, J. V. Ortiz, J. Cioslowski, D. J. Fox, Gaussian, Inc., Wallingford, CT, **2009**.
[50] M. Brandbyge, J.-L. Mozos, P. Ordejón, J. Taylor, K. Stokbro, *Phys. Rev. B* **2002**, *65*, 165401.
[51] J. Junquera, O. Paz, D. Sanchez-Portal, E. Artacho, *Phys. Rev. B* **2001**, *64*, 235111.
[52] J. P. Perdew, K. Burke, M. Ernzerhof, *Phys. Rev. Lett.* **1996**, *77*, 3865 – 3868.
[53] H. J. Monkhorst, J. D. Pack, *Phys. Rev. B* **1976**, *13*, 5188 – 5192.
[54] J. D. Pack, H. J. Monkhorst, *Phys. Rev. B* **1977**, *16*, 1748 – 1749.

Received: January 21, 2014
Published online on ■■ ■■, 2014

ARTICLES

Linker rectifiers induce directionality of interfacial electron transfer suitable for multi-electron reactions at electrode surfaces. The linkers have a terpyridyl group that can covalently bind Mn as in a well-known water oxidation catalyst and an acetylacetonate group that allows attachment to TiO_2 surfaces. The appropriate choice of the sense of the amide linkage suppresses back-electron transfer by shifting the transport channel away from the Fermi level.

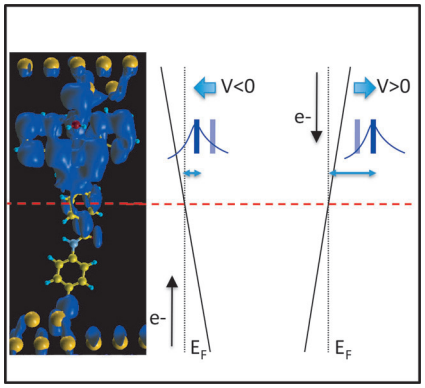

W. Ding, C. F. A. Negre, J. L. Palma, A. C. Durrell, L. J. Allen, K. J. Young, R. L. Milot, C. A. Schmuttenmaer, G. W. Brudvig,* R. H. Crabtree,* V. S. Batista**

■■ – ■■

Linker Rectifiers for Covalent Attachment of Transition-Metal Catalysts to Metal-Oxide Surfaces

CHEMPHYSCHEM

Supporting Information

Linker Rectifiers for Covalent Attachment of Transition-Metal Catalysts to Metal-Oxide Surfaces

Wendu Ding,[a, b] Christian F. A. Negre,[a, b] Julio L. Palma,[a] Alec C. Durrell,[a, b] Laura J. Allen,[a] Karin J. Young,[a] Rebecca L. Milot,[a] Charles A. Schmuttenmaer,*[a, b] Gary W. Brudvig,*[a, b] Robert H. Crabtree,*[a, b] and Victor S. Batista*[a, b]

cphc_201400063_sm_miscellaneous_information.pdf

Electronic Supporting Information

Linker Rectifiers for Covalent Attachment of Transition Metal Catalysts to Metal-Oxide Surfaces

Wendu Ding, Christian F. A. Negre, Julio L. Palma, Alec C. Durrell, Laura J. Allen, Karin J. Young, Rebecca L. Milot, Charles A. Schmuttenmaer*,Gary W. Brudvig*, Robert H. Crabtree*, and Victor S. Batista*

Yale University, Chemistry Department, P.O. Box 208107, New Haven, CT 06520–8107, USA

Energy Sciences Institute, Yale University, Yale University, P.O. Box 27394, West Haven, CT 06516-7394, USA

2/14/14

Table of Contents:

Figure S1: 1H NMR of 2-acetylpyridine pyridinium iodide S-2

Figure S2: ^{1}H NMR of nitrophenyl-terpyridine (**5**) S-3

Figure S3: ^{1}H NMR of aminophenyl-terpyridine (**6**) S-4

Figure S4: ^{1}H NMR of **L1-acac** S-5

Figure S5: ^{1}H NMR of nitrophenyl-acac (**8**) S-6

Figure S6: ^{1}H NMR of aminophenyl-acac (**9**) S-7

Figure S7: ^{1}H NMR **L2-acac**. S-8

Figure S8: ^{13}C NMR of **L2-acac** S-9

Figure S9: ORTEP diagram of **L1-acac** S-10

Table S1: Crystallograpic parameters for **L1-acac** S-11

Figure S10: ORTEP diagram of **L2-acac** S-12

Table S2: Crystallographic parameters for **L2-acac** S-13

Figure S11: Atominc structure of the leads used for IV curves simulations S-14

Figure S12: Schematic diagram of light-induced charge separation kinetics S-15

Figure S13: Schematic of slow recombination kinetics S-16

Table S3: Parameters of biexponetial fit to EPR kinetic data S-17

Figure S14: Biexponential fit to EPR kinetic data S-18

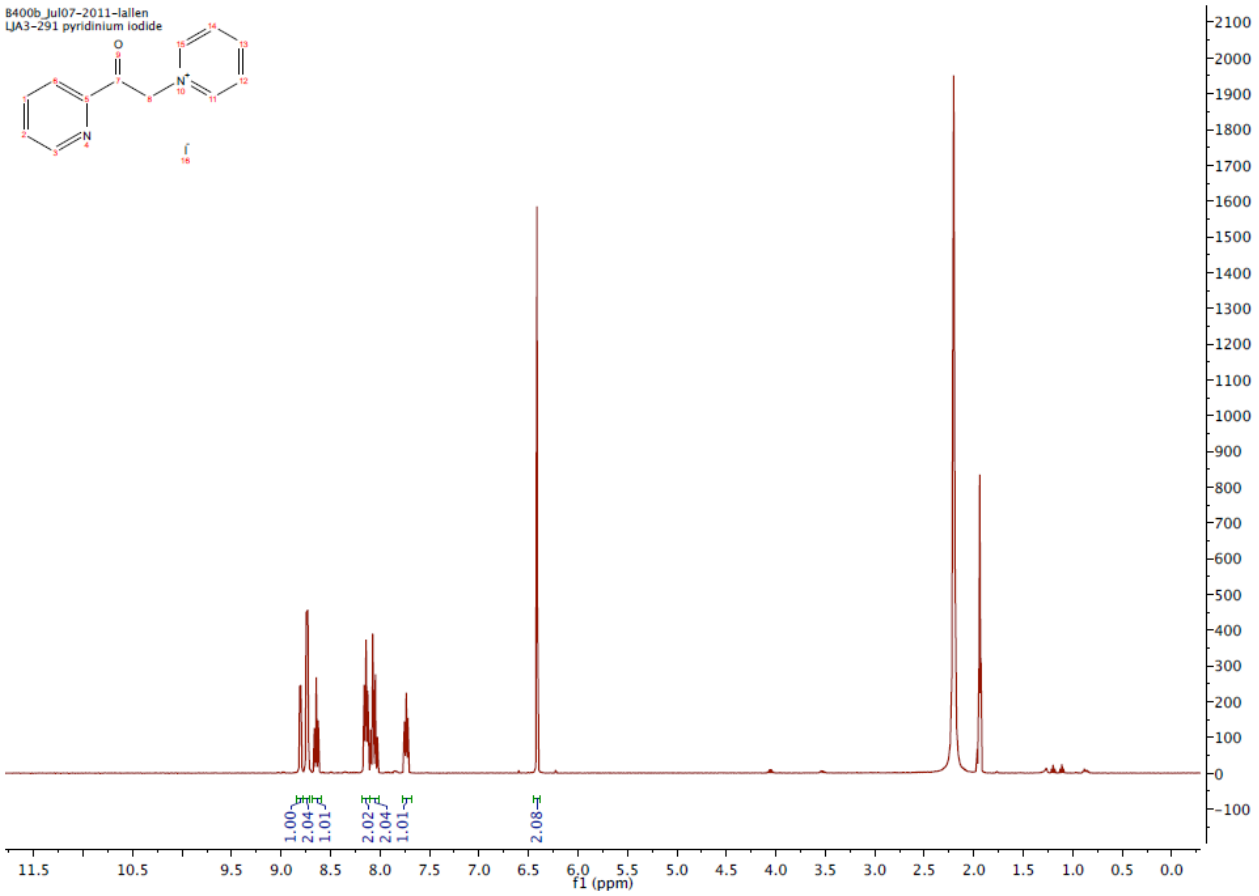

Figure S1: ^{1}H NMR of 2-acetylpyridine pyridinium iodide **4**

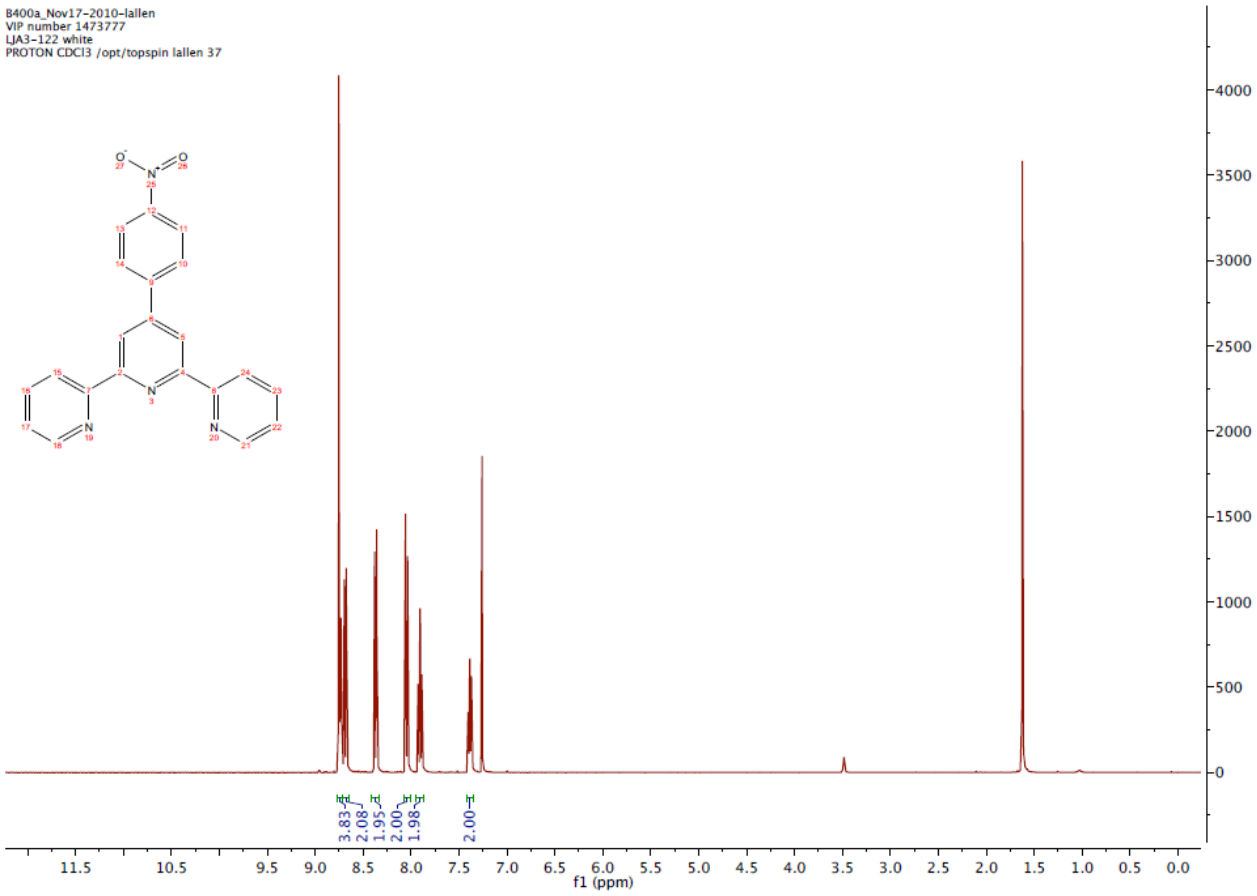

Figure S2: ^{1}H NMR of nitrophenyl-terpyridine (**5**)

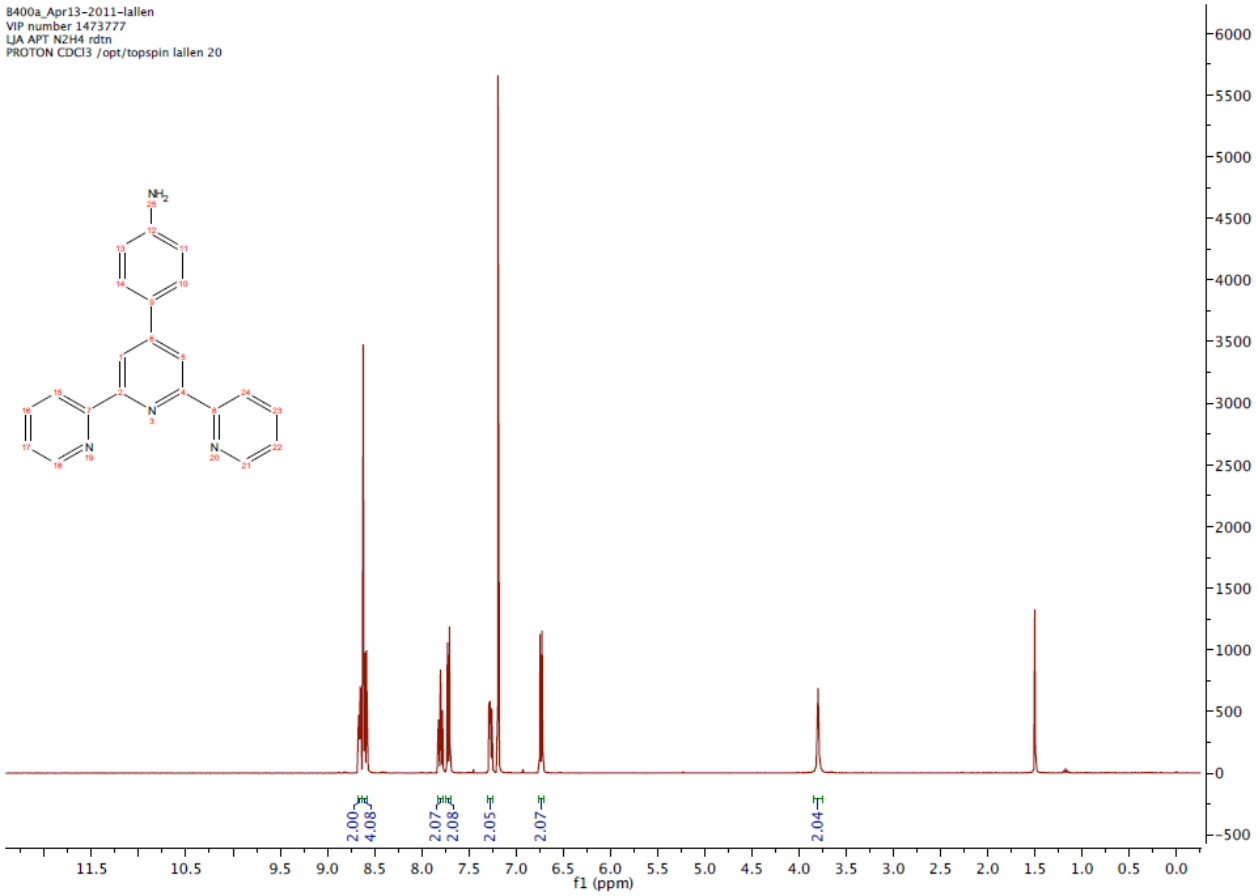

Figure S3: ^{1}H NMR of aminophenyl-terpyridine (**6**)

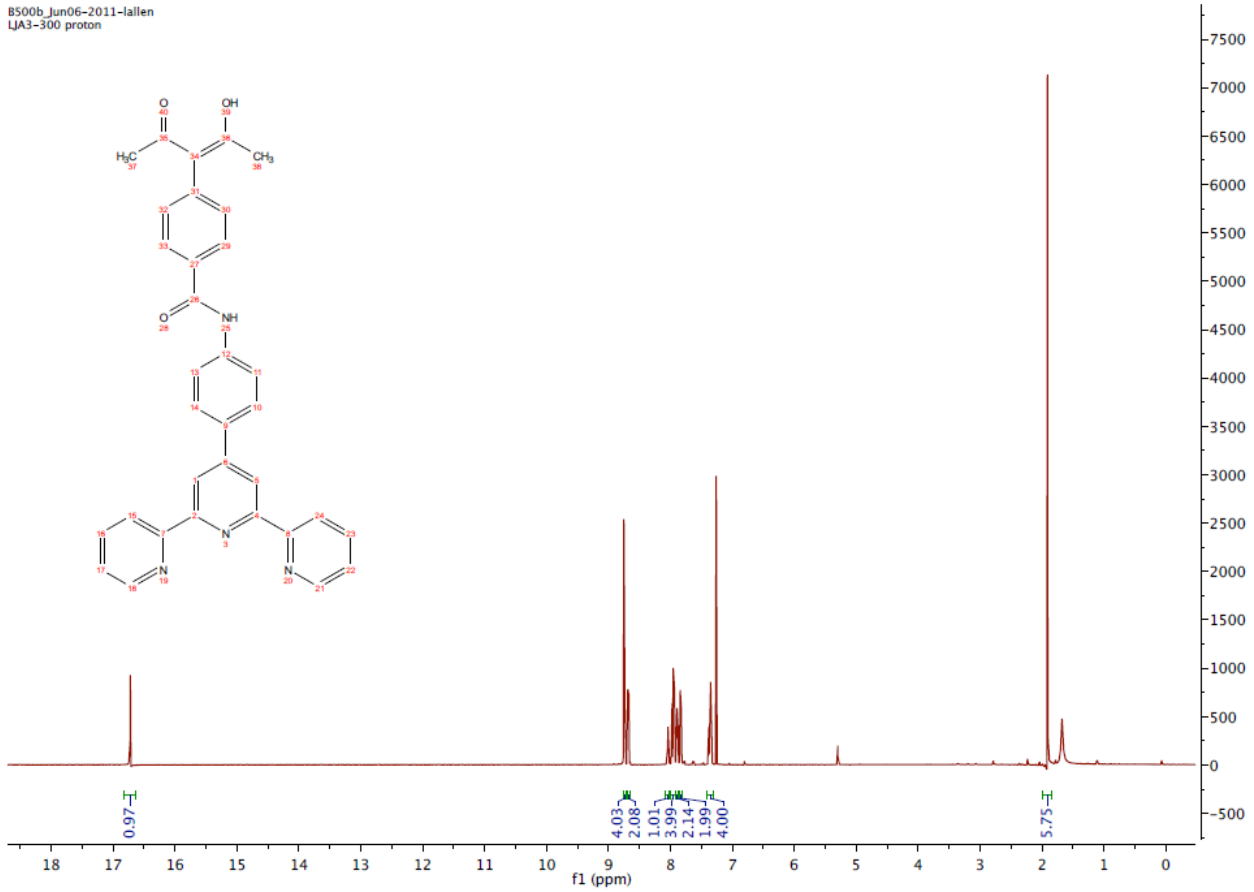

Figure S4: ^{1}H NMR of **L1-acac**

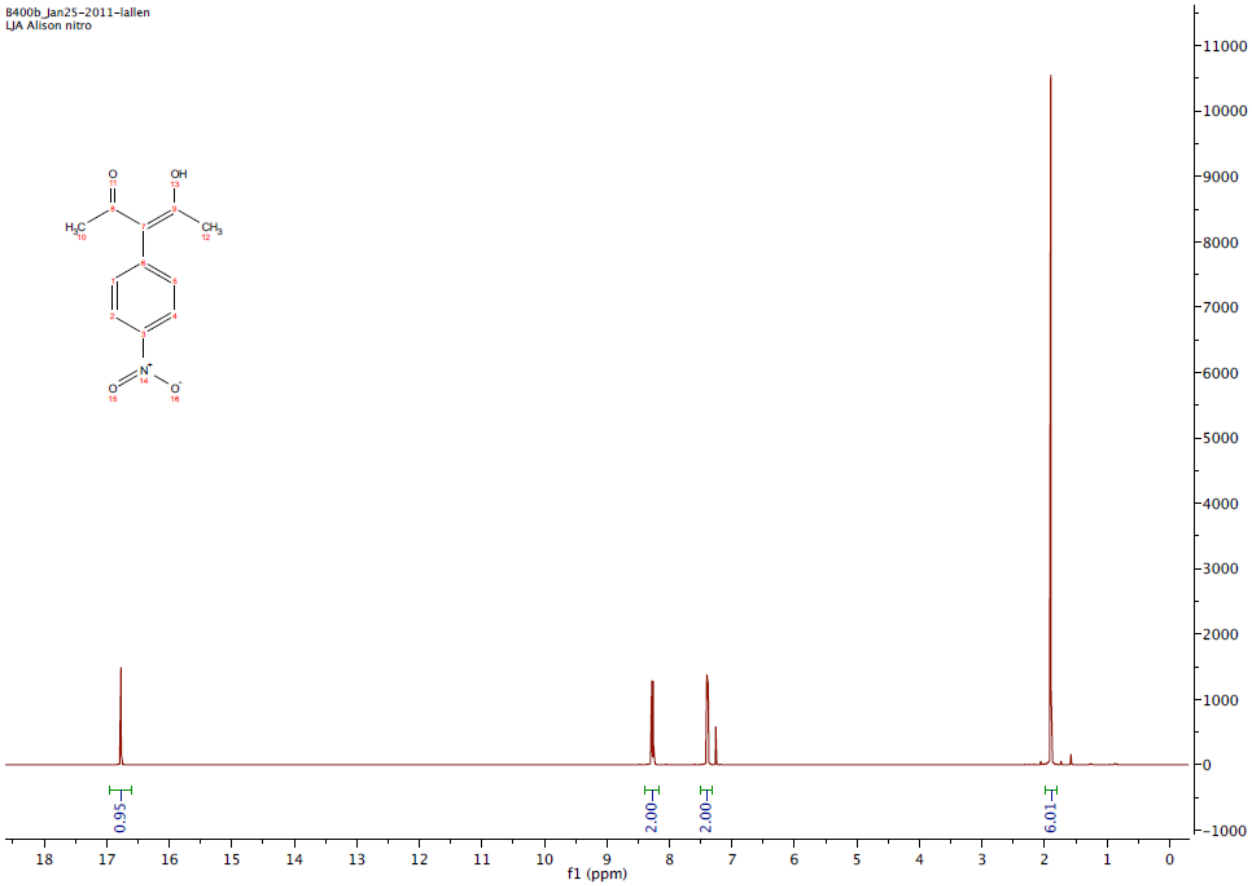

Figure S5: ^{1}H NMR of nitrophenyl-acac **8**

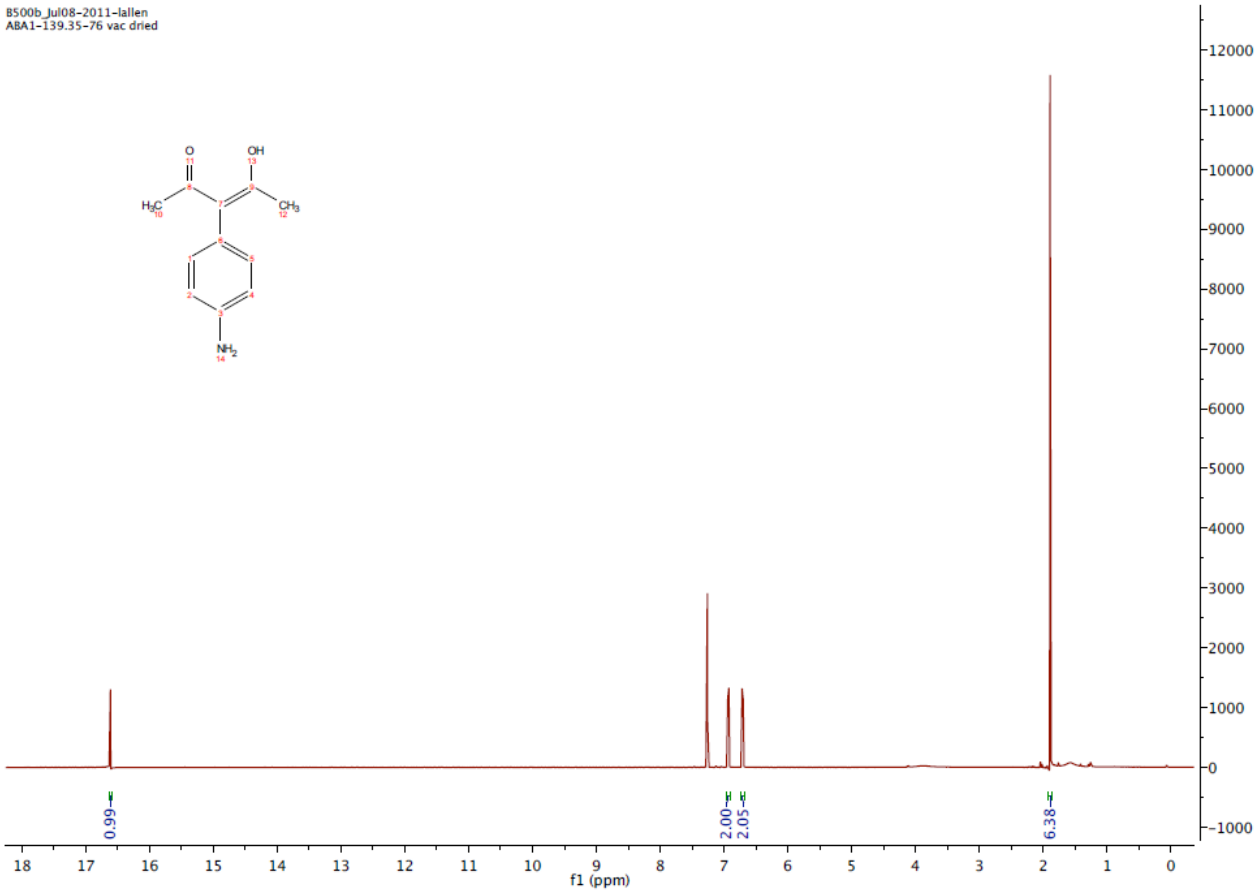

Figure S6: ^{1}H NMR of aminophenyl-acac **9**.

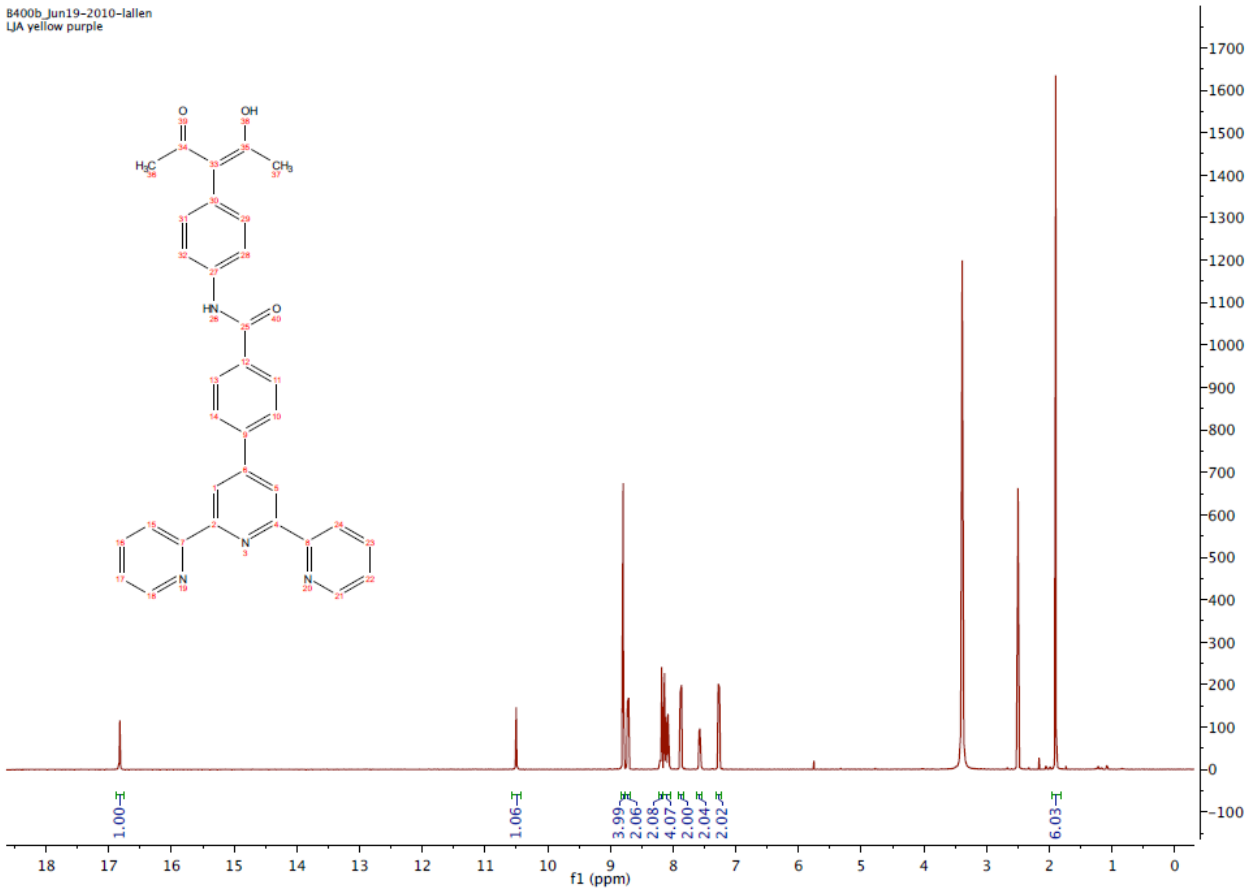

Figure S7: ^{1}H NMR **L2-acac**

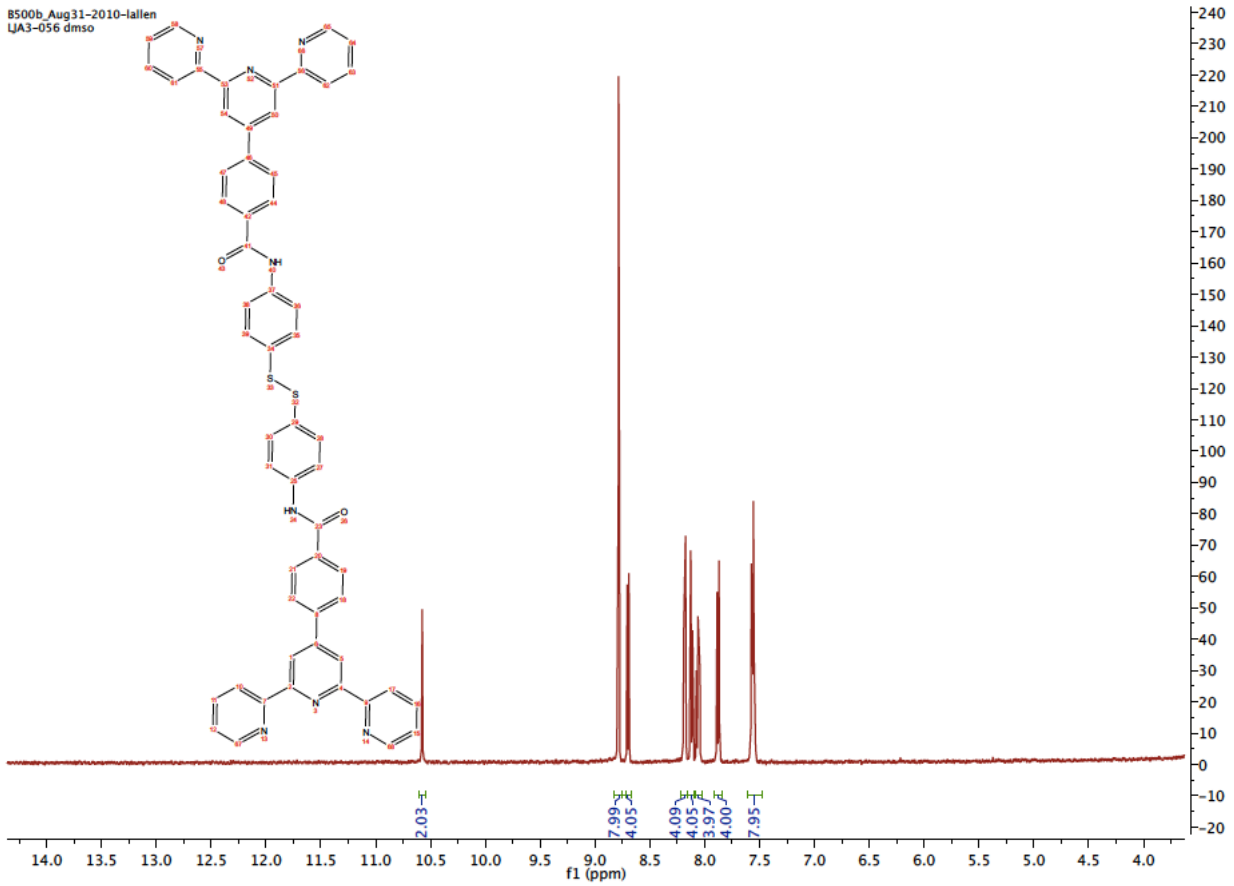

Figure S8: ^{13}C NMR of **L2-acac**

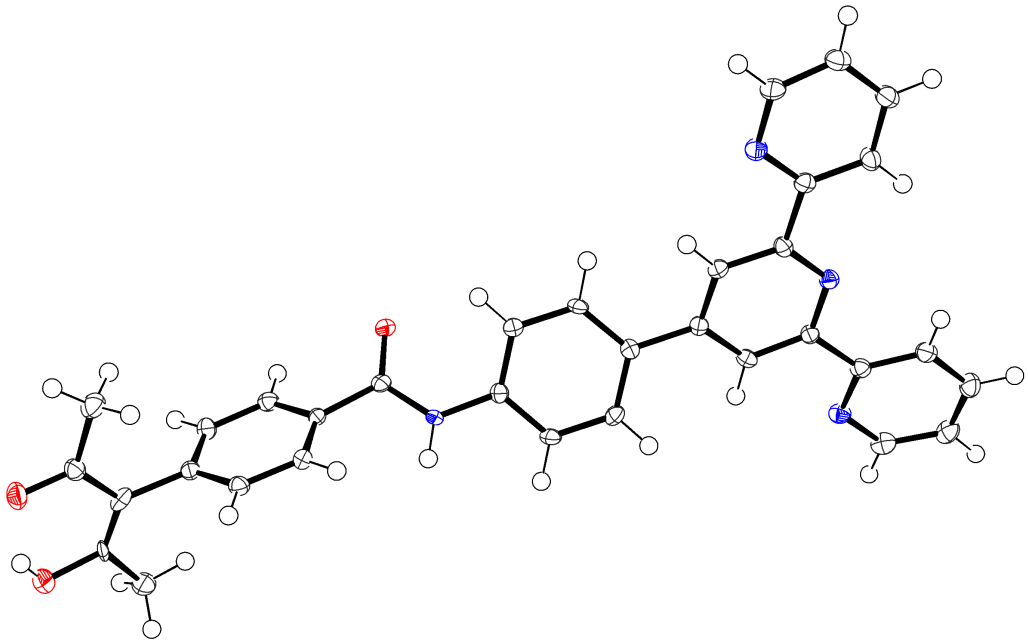

Figure S9: ORTEP diagram of **L1-acac**

Table S1: Crystallographic parameters for **L1-acac•**$2(C_6H_6)$

Empirical formula	$C_{45}H_{38}N_4O_3$
Fw	682.79
Radiation, λ, (Å)	MoKα, λ = 0.71073
T(K)	90 ± 2
Unit cell dimensions	
a (Å)	13.9169(8)
b (Å)	27.9498(15)
c (Å)	9.7140(5)
α (°)	90.00
β (°)	102.455(2)
γ (°)	90.00
V (Å^3)	3689.6(3)
Z	4
D_{calc} (g cm-3)	1.229
μ(MoKα) (mm^{-1})	0.078
Total, unique no. of refl.	61656, 7557
R_{int}	0.1543
No of param., restraints	472, 0
R^a, $R_w{}^b$	0.0617, 0.1530
G.O.F.	1.008
Resid. Density (e Å^{-3})	+ 0.554, -0.335

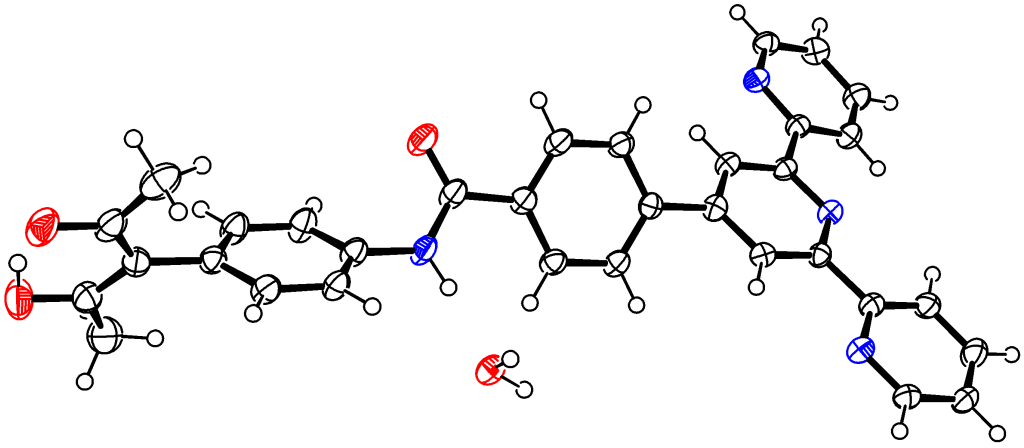

Figure S10: ORTEP diagram of **L2-acac**

Table S2: Crystallographic parameters for **L2-acac•**H_2O

Color, shape	Colorless, prism
Empirical formula	$C_{33}H_{28}O_4N_4$
Fw	544.61
Radiation, λ, Å	CuKα (λ = 1.54187 Å)
T(°C)	-180±1
Crystal system	monoclinic
Space group	$P2_1/C$
Unit cell dimensions	
a (Å)	17.1790(12)
b (Å)	10.51148(19)
c (Å)	16.7461(3)
α (°)	90
β (°)	111.207(8)
γ (°)	90
V (Å^3)	2819.2(2)
Z	4
Dcalc (g cm-3)	1.283
μ(CuKα) (cm^{-1})	6.953
Crystal size	0.50 x 0.44 x 0.30 mm
Total, unique no. of refl.	18706, 5011
R_{int}	0.034
No of param., restraints	387, 0
R^a, R_w^b	0.0505, 0.1674
G.O.F.	1.132
Resid. Density (e Å^{-3})	+0.27, -0.30

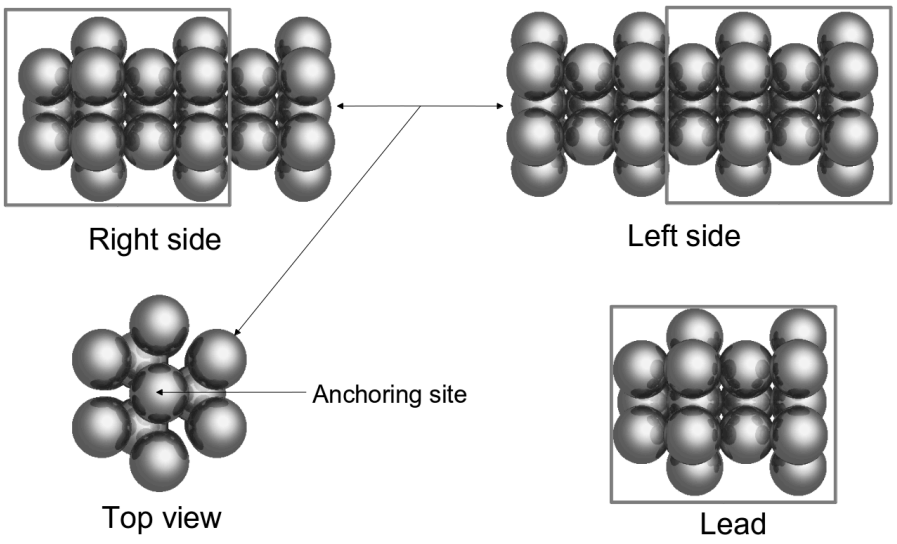

Figure S11: Scheme of the Leads used for building the extended molecule. We employed the Au lattice constant of 4.088 Å in an hcp lattice. The face of the leads is corresponds to a (111) surface.

Kinetic Model

As discussed in the SI of Ref. [34], we consider photoexcitation of an adsorbate molecule covalently bound to a semiconductor surface, a process that promotes an electron in the adsorbate from the ground to the excited state. We assume that the photoexcited state is isoenergetic with an electronic state in the semiconductor conduction band, inducing IET (see Fig. 5 of the manuscript).

The effective rate constant for electron injection is $k_{inj} = [p]k_{inj}^{*}$, where [p] is the effective concentration of photons as determined by the light intensity. The injection is typically ultrafast and is followed by forward electron transfer from terpyridine (T) to phenylacac (A), evolving the system from [1] to [2] with rate constant k_{12} and backward, from [2] to [1], with rate constant k_{21}. In addition, we assume that the hole left in the terpyridine ligand oxidizes Mn^{2+} to Mn^{3+} with an oxidation rate constant k_{23} and recombination k_{32}. Furthermore, [3] could recombine into [0] directly with rate constant k_r. We assume $k_{23} >> k_{32}$ to ensure a chemically sensible model, where Mn is rapidly oxidized by a hole localized in the phenylterpyridine ligand.

2. Quantitative Analysis of the EPR Signal

We find the rate constants k_{12} and k_{21} by considering the slow kinetics, monitored by EPR, after the initial pre-equilibrium of Mn^{II}-T-A-TiO_2 and Mn^{II}-T-A^{h+}-TiO_2^{e-} established by ultrafast injection and recombination:

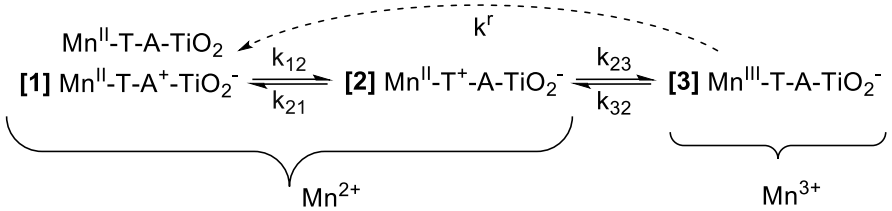

Figure S12. Schematic of the slow kinetics monitored by EPR, after the initial pre-equilibrium established, by ultrafast injection and recombination upon turning the light on.

According to Fig. S7, the kinetics equations are:

$$\begin{aligned}\frac{d[1]}{dt} &= -k_{12}[1] + k_{21}[2] + k_r[3] \\ \frac{d[2]}{dt} &= k_{12}[1] - k_{21}[2] - k_{23}[2] + k_{32}[3] \\ \frac{d[3]}{dt} &= k_{23}[2] - (k_{32} + k_r)[3]\end{aligned} \qquad (3)$$

When p(0)=[1]+[2]+[3], we obtain:

$$\begin{aligned}\frac{d[1]}{dt} &= -k_{12}[1] + k_{21}(p(0) - [1] - [3]) + k_r[3] \\ \frac{d[3]}{dt} &= k_{23}(p(0) - [1] - [3]) - (k_{32} + k_r)[3]\end{aligned} \qquad (4)$$

with

$$\frac{d[1]}{dt} = -k_{11}[1] + k_{13}[3] + k_{21}p(0)$$
$$\frac{d[3]}{dt} = -k_{33}[3] + k_{31}[1] + k_{23}p(0) \quad (5)$$

where $k_{11}=k_{21}+k_{12}$, $k_{13}= k_r-k_{21}$, $k_{33}=k_r+k_{32}+k_{23}$, and $k_{31}=-k_{23}$.

Solving for [1], from Eq. (5), we obtain:

$$[1] = k_{31}^{-1}\frac{d[3]}{dt} + k_{31}^{-1}k_{33}[3] - k_{31}^{-1}k_{23}p(0)$$
$$\frac{d[1]}{dt} = k_{31}^{-1}\frac{d^2[3]}{dt^2} + k_{31}^{-1}k_{33}\frac{d[3]}{dt} \quad (6)$$
$$= -k_{11}k_{31}^{-1}\frac{d[3]}{dt} + (k_{13} - k_{11}k_{31}^{-1}k_{33})[3] + (k_{21} + k_{11}k_{31}^{-1}k_{23})p(0)$$

Associating terms, we obtain:

$$\frac{d^2[3]}{dt^2} + (k_{33} + k_{11})\frac{d[3]}{dt} + (k_{11}k_{33} - k_{13}k_{31})[3] - (k_{31}k_{21} + k_{11}k_{23})p(0) = 0 \quad (7)$$

or

$$\frac{d^2[3]}{dt^2} + A\frac{d[3]}{dt} + B[3] - C = 0 \quad (8)$$

with $A = k_{33}+k_{11}$, $B=k_{33}k_{11}-k_{13}\,k_{31}$ and $C=(k_{11}k_{23}+k_{31}k_{21})p(0)$, with solution

$$[3] = A_1 e^{-k^{(+)}t} + A_2 e^{-k^{(-)}t} + \frac{C}{B} \quad (9)$$

where

$$k^{(\pm)} = \frac{A \pm \sqrt{A^2 - 4B}}{2} \quad (10)$$

with $A= k^{(-)}+k^{(+)}$ and $B= k^{(-)}k^{(+)}$.

We note that for the case of light OFF, $k_{inj} = 0$ since [p] = 0. In addition, $[Mn^{II}\text{-T-}A^{h+}\text{-}TiO_2^{e-}] = 0$, since the transition from $[Mn^{II}\text{-T-}A^{h+}\text{-}TiO_2^{e-}]$ to $[Mn^{II}TATiO_2]$ is ultrafast. Therefore, the resulting kinetic model is analogous to the light-on model but with an effective kinetic constant $k_{12} = 0$:

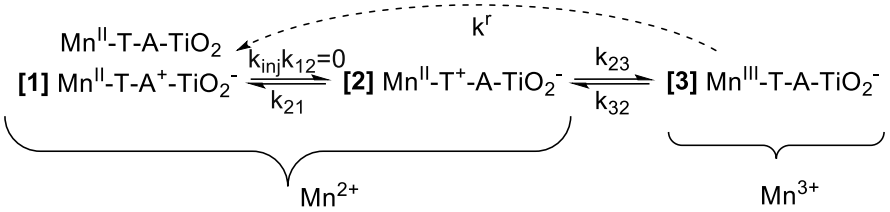

Figure S13. Schematics of the slow recombination kinetics monitored by EPR after turning the light off.

For the case of light OFF (k_{12}=0), $k^{(-)OFF}$= (42.16 s)$^{-1}$ and $k^{(+)OFF}$ = (9.18 s)$^{-1}$, while for light ON, we obtain $k^{(-)OFF}$= (14.1 s)$^{-1}$ and $k^{(-)OFF}$ = (3.0 s)$^{-1}$.
Assuming that $k_{23} >> k_{32} \approx 0$, we solve for k_r and k_{23}, giving:

$$k_{23} = \frac{(k^{(-)OFF} + k^{(+)OFF})\, k_{21} - k_{21}^2 - k^{(-)OFF} k^{(+)OFF}}{k_{21}}$$
$$k_r = \frac{k^{(-)OFF} k^{(+)OFF}}{k_{21}} \qquad (11)$$

For the case of light-on, we have $k^{(-)ON}$=(14.11 s)$^{-1}$ and $k^{(+)ON}$=(3.04 s)$^{-1}$, and solving for k_{12} and k_{21}, we obtain:

$$k_{12} = (k^{(-)ON} + k^{(+)ON}) - (k^{(-)OFF} + k^{(+)OFF})$$
$$k_{21} = \frac{\left(k^{(-)OFF}\right)^2 + \left(k^{(-)OFF} + k^{(+)OFF}\right)\left(k^{(+)OFF} - k^{(+)ON} - k^{(-)ON}\right) + k^{(-)ON} k^{(+)ON}}{k^{(-)OFF} + k^{(+)OFF} - k^{(-)ON} - k^{(+)ON}} \qquad (12)$$

giving k_{12}=0.272 s^{-1} and k_{21} = 0.0546 s^{-1} (*i.e.*, $K_1 \approx 5$, as indicated in Sec. 1). Substituting these values into Eq. (11) we obtain, k_{23}=0.0307 s^{-1} and k_r = 0.0472 s^{-1}.

We obtain [3] as a function of time by using Eq. (9), with parameters given in Table 1, with A_1 and A_2 obtained by making [3]=[2]=0 at t=0. We solve for [2], as a function of [3], from Eq. (3), and for [1] as a function of [3] from p(0)=[1]+[2]+[3]. Figure 5 of the text shows [1], [2] and [3] as a function of time.

Table S3: Parameters of the bi-exponential fits to the experimental EPR signal, modeled as $EPR = A_1 e^{-k^{(+)}t} + A_2 e^{-k^{(-)}t} + A_0$

	Light-On	Light-Off
A_0	241.8	-189.0
$k^{(+)}$	(14.1 s)$^{-1}$	(42.2 s)$^{-1}$
A_2	328.4	-456.2
$k^{(-)}$	(3.0 s)$^{-1}$	(9.2 s)$^{-1}$
A_4	5220.9	5794.5
Corr. Coeff.	0.998	0.999
EMS rel. error	0.210	7.263

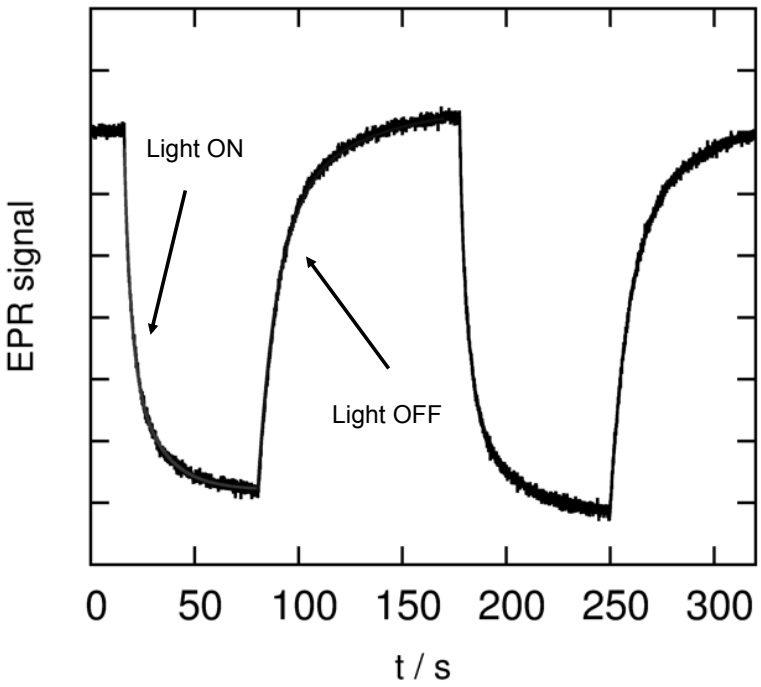

Figure S14: EPR signal and biexponential fit for light-on and light-off.

Figure S14 shows that the relaxation dynamics upon turning the light ON/OFF can be properly described by a bi-exponential function, as predicted by the kinetic model with parameters listed in Table 1. From the parameters of the biexponential fit, the remaining rate constants suggested by the model shown in Fig. 1 may be calculated.

For the case of light OFF (k_{12}=0), $k^{(-)OFF}$= (42.16 s)$^{-1}$ and $k^{(+)OFF}$ = (9.18 s)$^{-1}$, while for light ON, we obtain $k^{(-)OFF}$= (14.1 s)$^{-1}$ and $k^{(-)OFF}$ = (3.0 s)$^{-1}$. Assuming that kr can be neglected, we solve for k23 and k32, giving:

$$\begin{aligned} k_{23} &= \frac{(k^{(-)OFF} + k^{(+)OFF})\, k_{21} - k_{21}^2 - k^{(-)OFF} k^{(+)OFF}}{k_{21}} \\ k_{32} &= \frac{k^{(-)OFF} k^{(+)OFF}}{k_{21}} \end{aligned} \tag{11}$$

For the case of light-on, we have $k^{(-)ON}$=(14.11 s)$^{-1}$ and $k^{(+)ON}$=(3.04 s)$^{-1}$, and solving for k_{12} and k_{21}, we obtain:

$$\begin{aligned} k_{12} &= (k^{(-)ON} + k^{(+)ON}) - (k^{(-)OFF} + k^{(+)OFF}) \\ k_{21} &= \frac{\left(k^{(-)OFF}\right)^2 + \left(k^{(-)OFF} + k^{(+)OFF}\right)\left(k^{(+)OFF} - k^{(+)ON} - k^{(-)ON}\right) + k^{(-)ON} k^{(+)ON}}{k^{(-)OFF} + k^{(+)OFF} - k^{(-)ON} - k^{(+)ON}} \end{aligned} \tag{12}$$

giving k_{12}=0.272 s^{-1} and k_{21} = 0.0546 s^{-1} (*i.e.*, K_1=5). Substituting these values into Eq. (11) we obtain, k_{23}=0.0307 s^{-1} and k_{32} = 0.0472 s^{-1}.

Coordinates for extended systems used in this study:

Au-Mn-terpy-L1-Au

Au	0.00000000	-4.99573000	0.00000000
Au	2.88429000	-4.99573000	0.00000000
Au	5.76858000	-4.99573000	0.00000000
Au	8.65286000	-4.99573000	0.00000000
Au	-1.44214000	-2.49786000	0.00000000
Au	1.44214000	-2.49786000	0.00000000
Au	4.32643000	-2.49786000	0.00000000
Au	7.21072000	-2.49786000	0.00000000
Au	-2.88429000	0.00000000	0.00000000
Au	0.00000000	0.00000000	0.00000000
Au	2.88428000	0.00000000	0.00000000
Au	5.76858000	0.00001000	0.00000000
Au	-4.32644000	2.49786000	0.00000000
Au	-1.44215000	2.49786000	0.00000000
Au	1.44214000	2.49786000	0.00000000
Au	4.32643000	2.49787000	0.00000000
Au	-0.00001000	-3.33049000	2.35502000
Au	2.88429000	-3.33049000	2.35502000
Au	5.76857000	-3.33049000	2.35502000
Au	8.65287000	-3.33048000	2.35502000
Au	-1.44215000	-0.83262000	2.35502000
Au	1.44214000	-0.83262000	2.35502000
Au	4.32643000	-0.83262000	2.35502000
Au	7.21072000	-0.83262000	2.35502000
Au	-2.88429000	1.66524000	2.35502000
Au	-0.00001000	1.66524000	2.35502000
Au	2.88429000	1.66525000	2.35502000
Au	5.76857000	1.66525000	2.35502000
Au	-4.32645000	4.16311000	2.35502000
Au	-1.44215000	4.16311000	2.35502000
Au	1.44213000	4.16311000	2.35502000
Au	4.32643000	4.16312000	2.35502000
Au	-1.44214000	-4.16312000	4.71004000
Au	1.44214000	-4.16312000	4.71004000
Au	4.32643000	-4.16310000	4.71004000
Au	7.21072000	-4.16310000	4.71004000
Au	-2.88429000	-1.66525000	4.71004000
Au	0.00000000	-1.66525000	4.71004000
Au	2.88429000	-1.66524000	4.71004000
Au	5.76857000	-1.66524000	4.71004000
Au	-4.32644000	0.83262000	4.71004000
Au	-1.44215000	0.83262000	4.71004000
Au	1.44214000	0.83263000	4.71004000
Au	4.32643000	0.83263000	4.71004000
Au	-5.76858000	3.33048000	4.71004000
Au	-2.88429000	3.33049000	4.71004000
Au	-0.00001000	3.33050000	4.71004000
Au	2.88428000	3.33050000	4.71004000
Au	0.00000000	-4.99573000	7.06505000
Au	2.88429000	-4.99573000	7.06505000
Au	5.76858000	-4.99573000	7.06505000
Au	8.65286000	-4.99573000	7.06505000
Au	-1.44214000	-2.49786000	7.06505000

Au	1.44214000	-2.49786000	7.06505000
Au	4.32643000	-2.49786000	7.06505000
Au	7.21072000	-2.49786000	7.06505000
Au	-2.88429000	0.00000000	7.06505000
Au	0.00000000	0.00000000	7.06505000
Au	2.88428000	0.00000000	7.06505000
Au	5.76858000	0.00001000	7.06505000
Au	-4.32644000	2.49786000	7.06505000
Au	-1.44215000	2.49786000	7.06505000
Au	1.44214000	2.49786000	7.06505000
Au	4.32643000	2.49787000	7.06505000
Au	-0.00001000	-3.33049000	9.42006000
Au	2.88429000	-3.33049000	9.42006000
Au	5.76857000	-3.33049000	9.42006000
Au	8.65287000	-3.33048000	9.42006000
Au	-1.44215000	-0.83262000	9.42006000
Au	1.44214000	-0.83262000	9.42006000
Au	4.32643000	-0.83262000	9.42006000
Au	7.21072000	-0.83262000	9.42006000
Au	-2.88429000	1.66524000	9.42006000
Au	-0.00001000	1.66524000	9.42006000
Au	2.88429000	1.66525000	9.42006000
Au	5.76857000	1.66525000	9.42006000
Au	-4.32645000	4.16311000	9.42006000
Au	-1.44215000	4.16311000	9.42006000
Au	1.44213000	4.16311000	9.42006000
Au	4.32643000	4.16312000	9.42006000
Au	-1.44214000	-4.16312000	11.77507000
Au	1.44214000	-4.16312000	11.77507000
Au	4.32643000	-4.16310000	11.77507000
Au	7.21072000	-4.16310000	11.77507000
Au	-2.88429000	-1.66525000	11.77507000
Au	0.00000000	-1.66525000	11.77507000
Au	2.88429000	-1.66524000	11.77507000
Au	5.76857000	-1.66524000	11.77507000
Au	-4.32644000	0.83262000	11.77507000
Au	-1.44215000	0.83262000	11.77507000
Au	1.44214000	0.83263000	11.77507000
Au	4.32643000	0.83263000	11.77507000
Au	-5.76858000	3.33048000	11.77507000
Au	-2.88429000	3.33049000	11.77507000
Au	-0.00001000	3.33050000	11.77507000
Au	2.88428000	3.33050000	11.77507000
Au	0.00000000	0.00000000	14.13008000
Au	-1.44215000	2.49786000	14.13008000
Au	1.44214000	2.49786000	14.13008000
S	0.00284399	-1.88530461	15.48212233
H	2.64416995	-3.38431680	16.27177722
H	-2.40415828	-0.14095483	16.54282704
O	1.42900999	0.21584230	16.78704089
H	2.39500799	0.28109205	16.81482011
H	1.09518082	1.12223862	16.85978664
H	4.74075818	-4.55701004	16.94355415
C	2.97885795	-3.37351213	17.30558258
H	-4.29248000	1.22187034	17.43546506
C	-2.45469884	0.11203463	17.59848394
O	-0.97045798	-3.54049940	17.59875926
Mn	0.29283574	-1.60012343	17.66769299

C	4.14876409	-4.02751189	17.68182636
H	-0.59803136	-4.41022607	17.80609396
H	-1.89252442	-3.56406504	17.89442521
C	-3.50827779	0.87264652	18.09801371
N	2.20251586	-2.69953785	18.17530710
N	-1.45276306	-0.35047313	18.37046803
C	4.52704715	-3.97724285	19.02433000
H	5.43211728	-4.47183623	19.36266147
C	-3.51878312	1.16518430	19.46263974
C	2.56365717	-2.64721102	19.48580598
C	-1.45523027	-0.06840933	19.70131164
N	0.58029299	-1.33386458	19.77826363
H	-4.32074823	1.75449659	19.89599200
C	3.72799916	-3.28233081	19.93217583
C	-2.48414900	0.69129238	20.26920417
C	1.65163415	-1.88432183	20.38928407
C	-0.31074204	-0.61180136	20.49172506
H	4.01585227	-3.23934152	20.97520926
H	-2.48663715	0.91519468	21.32871132
C	1.86646211	-1.72349800	21.75325806
C	-0.15188451	-0.41667553	21.85840136
H	2.74714210	-2.14237522	22.22126263
H	-0.89126452	0.13638531	22.42149688
C	0.95863598	-0.97274720	22.53874217
C	1.15409998	-0.77767957	23.97319520
H	0.08420813	1.10899671	24.07958014
H	2.29015875	-2.60491627	24.30344881
C	0.61717136	0.34677008	24.63969341
C	1.88573300	-1.70328583	24.75309850
C	0.78938444	0.55509365	25.99843478
C	2.05448033	-1.51841441	26.11316993
H	0.37819761	1.42983200	26.48118650
H	2.59979893	-2.26114595	26.68923381
C	1.51351724	-0.38572915	26.76695406
N	1.73557973	-0.25615310	28.12765383
H	2.27369613	-0.99695980	28.55669990
O	0.44125671	1.57324385	28.62658464
C	1.23438644	0.72222822	29.00421738
H	3.57607369	-0.45028934	30.03406330
C	1.72099125	0.62877313	30.41133080
C	2.91760671	-0.01186162	30.77979028
H	0.02553574	1.75410035	31.10317673
C	0.93773442	1.24781123	31.39996554
C	3.31349945	-0.04394983	32.11731624
H	4.24521745	-0.52800907	32.39300929
C	1.33204445	1.20569637	32.73584086
C	2.51833011	0.55816659	33.09717326
H	0.71708650	1.67872319	33.49506109
S	3.02425236	0.51110683	34.80311231
Au	1.44214000	-4.16312000	35.56499000
Au	4.32643000	-4.16312000	35.56499000
Au	2.88428000	-1.66525000	35.56499000
Au	0.00000000	-4.99574000	37.92000000
Au	2.88429000	-4.99574000	37.92000000
Au	5.76858000	-4.99574000	37.92000000
Au	8.65287000	-4.99574000	37.92000000
Au	-1.44215000	-2.49788000	37.92000000
Au	1.44214000	-2.49788000	37.92000000

Au	4.32643000	-2.49788000	37.92000000
Au	7.21072000	-2.49788000	37.92000000
Au	-2.88429000	-0.00001000	37.92000000
Au	0.00000000	-0.00001000	37.92000000
Au	2.88429000	-0.00001000	37.92000000
Au	5.76858000	-0.00001000	37.92000000
Au	-4.32644000	2.49786000	37.92000000
Au	-1.44215000	2.49786000	37.92000000
Au	1.44214000	2.49786000	37.92000000
Au	4.32643000	2.49786000	37.92000000
Au	0.00000000	-3.33050000	40.27501000
Au	2.88429000	-3.33050000	40.27501000
Au	5.76857000	-3.33050000	40.27501000
Au	8.65286000	-3.33050000	40.27501000
Au	-1.44214000	-0.83263000	40.27501000
Au	1.44215000	-0.83263000	40.27501000
Au	4.32644000	-0.83263000	40.27501000
Au	7.21071000	-0.83263000	40.27501000
Au	-2.88429000	1.66523000	40.27501000
Au	0.00000000	1.66523000	40.27501000
Au	2.88429000	1.66523000	40.27501000
Au	5.76858000	1.66523000	40.27501000
Au	-4.32644000	4.16310000	40.27501000
Au	-1.44215000	4.16310000	40.27501000
Au	1.44214000	4.16310000	40.27501000
Au	4.32643000	4.16310000	40.27501000
Au	-1.44215000	-4.16312000	42.63002000
Au	1.44214000	-4.16312000	42.63002000
Au	4.32643000	-4.16312000	42.63002000
Au	7.21072000	-4.16312000	42.63002000
Au	-2.88428000	-1.66526000	42.63002000
Au	-0.00001000	-1.66525000	42.63002000
Au	2.88428000	-1.66525000	42.63002000
Au	5.76857000	-1.66525000	42.63002000
Au	-4.32643000	0.83261000	42.63002000
Au	-1.44214000	0.83261000	42.63002000
Au	1.44214000	0.83262000	42.63002000
Au	4.32643000	0.83262000	42.63002000
Au	-5.76858000	3.33048000	42.63002000
Au	-2.88429000	3.33048000	42.63002000
Au	0.00000000	3.33048000	42.63002000
Au	2.88428000	3.33048000	42.63002000
Au	0.00000000	-4.99574000	44.98504000
Au	2.88429000	-4.99574000	44.98504000
Au	5.76858000	-4.99574000	44.98504000
Au	8.65287000	-4.99574000	44.98504000
Au	-1.44215000	-2.49788000	44.98504000
Au	1.44214000	-2.49788000	44.98504000
Au	4.32643000	-2.49788000	44.98504000
Au	7.21072000	-2.49788000	44.98504000
Au	-2.88429000	-0.00001000	44.98504000
Au	0.00000000	-0.00001000	44.98504000
Au	2.88429000	-0.00001000	44.98504000
Au	5.76858000	-0.00001000	44.98504000
Au	-4.32644000	2.49786000	44.98504000
Au	-1.44215000	2.49786000	44.98504000
Au	1.44214000	2.49786000	44.98504000
Au	4.32643000	2.49786000	44.98504000

Au	0.00000000	-3.33050000	47.34005000
Au	2.88429000	-3.33050000	47.34005000
Au	5.76857000	-3.33050000	47.34005000
Au	8.65286000	-3.33050000	47.34005000
Au	-1.44214000	-0.83263000	47.34005000
Au	1.44215000	-0.83263000	47.34005000
Au	4.32644000	-0.83263000	47.34005000
Au	7.21071000	-0.83263000	47.34005000
Au	-2.88429000	1.66523000	47.34005000
Au	0.00000000	1.66523000	47.34005000
Au	2.88429000	1.66523000	47.34005000
Au	5.76858000	1.66523000	47.34005000
Au	-4.32644000	4.16310000	47.34005000
Au	-1.44215000	4.16310000	47.34005000
Au	1.44214000	4.16310000	47.34005000
Au	4.32643000	4.16310000	47.34005000
Au	-1.44215000	-4.16312000	49.69506000
Au	1.44214000	-4.16312000	49.69506000
Au	4.32643000	-4.16312000	49.69506000
Au	7.21072000	-4.16312000	49.69506000
Au	-2.88428000	-1.66526000	49.69506000
Au	-0.00001000	-1.66525000	49.69506000
Au	2.88428000	-1.66525000	49.69506000
Au	5.76857000	-1.66525000	49.69506000
Au	-4.32643000	0.83261000	49.69506000
Au	-1.44214000	0.83261000	49.69506000
Au	1.44214000	0.83262000	49.69506000
Au	4.32643000	0.83262000	49.69506000
Au	-5.76858000	3.33048000	49.69506000
Au	-2.88429000	3.33048000	49.69506000
Au	0.00000000	3.33048000	49.69506000
Au	2.88428000	3.33048000	49.69506000

Au-Mn-terpy-L2-Au

Au	0.00000000	-4.99573000	0.00000000
Au	2.88429000	-4.99573000	0.00000000
Au	5.76858000	-4.99573000	0.00000000
Au	8.65286000	-4.99573000	0.00000000
Au	-1.44214000	-2.49786000	0.00000000
Au	1.44214000	-2.49786000	0.00000000
Au	4.32643000	-2.49786000	0.00000000
Au	7.21072000	-2.49786000	0.00000000
Au	-2.88429000	0.00000000	0.00000000
Au	0.00000000	0.00000000	0.00000000
Au	2.88428000	0.00000000	0.00000000
Au	5.76858000	0.00001000	0.00000000
Au	-4.32644000	2.49786000	0.00000000
Au	-1.44215000	2.49786000	0.00000000
Au	1.44214000	2.49786000	0.00000000
Au	4.32643000	2.49787000	0.00000000
Au	-0.00001000	-3.33049000	2.35502000
Au	2.88429000	-3.33049000	2.35502000
Au	5.76857000	-3.33049000	2.35502000
Au	8.65287000	-3.33048000	2.35502000
Au	-1.44215000	-0.83262000	2.35502000
Au	1.44214000	-0.83262000	2.35502000
Au	4.32643000	-0.83262000	2.35502000

Au	7.21072000	-0.83262000	2.35502000
Au	-2.88429000	1.66524000	2.35502000
Au	-0.00001000	1.66524000	2.35502000
Au	2.88429000	1.66525000	2.35502000
Au	5.76857000	1.66525000	2.35502000
Au	-4.32645000	4.16311000	2.35502000
Au	-1.44215000	4.16311000	2.35502000
Au	1.44213000	4.16311000	2.35502000
Au	4.32643000	4.16312000	2.35502000
Au	-1.44214000	-4.16312000	4.71004000
Au	1.44214000	-4.16312000	4.71004000
Au	4.32643000	-4.16310000	4.71004000
Au	7.21072000	-4.16310000	4.71004000
Au	-2.88429000	-1.66525000	4.71004000
Au	0.00000000	-1.66525000	4.71004000
Au	2.88429000	-1.66524000	4.71004000
Au	5.76857000	-1.66524000	4.71004000
Au	-4.32644000	0.83262000	4.71004000
Au	-1.44215000	0.83262000	4.71004000
Au	1.44214000	0.83263000	4.71004000
Au	4.32643000	0.83263000	4.71004000
Au	-5.76858000	3.33048000	4.71004000
Au	-2.88429000	3.33049000	4.71004000
Au	-0.00001000	3.33050000	4.71004000
Au	2.88428000	3.33050000	4.71004000
Au	0.00000000	-4.99573000	7.06505000
Au	2.88429000	-4.99573000	7.06505000
Au	5.76858000	-4.99573000	7.06505000
Au	8.65286000	-4.99573000	7.06505000
Au	-1.44214000	-2.49786000	7.06505000
Au	1.44214000	-2.49786000	7.06505000
Au	4.32643000	-2.49786000	7.06505000
Au	7.21072000	-2.49786000	7.06505000
Au	-2.88429000	0.00000000	7.06505000
Au	0.00000000	0.00000000	7.06505000
Au	2.88428000	0.00000000	7.06505000
Au	5.76858000	0.00001000	7.06505000
Au	-4.32644000	2.49786000	7.06505000
Au	-1.44215000	2.49786000	7.06505000
Au	1.44214000	2.49786000	7.06505000
Au	4.32643000	2.49787000	7.06505000
Au	-0.00001000	-3.33049000	9.42006000
Au	2.88429000	-3.33049000	9.42006000
Au	5.76857000	-3.33049000	9.42006000
Au	8.65287000	-3.33048000	9.42006000
Au	-1.44215000	-0.83262000	9.42006000
Au	1.44214000	-0.83262000	9.42006000
Au	4.32643000	-0.83262000	9.42006000
Au	7.21072000	-0.83262000	9.42006000
Au	-2.88429000	1.66524000	9.42006000
Au	-0.00001000	1.66524000	9.42006000
Au	2.88429000	1.66525000	9.42006000
Au	5.76857000	1.66525000	9.42006000
Au	-4.32645000	4.16311000	9.42006000
Au	-1.44215000	4.16311000	9.42006000
Au	1.44213000	4.16311000	9.42006000
Au	4.32643000	4.16312000	9.42006000
Au	-1.44214000	-4.16312000	11.77507000

Au	1.44214000	-4.16312000	11.77507000
Au	4.32643000	-4.16310000	11.77507000
Au	7.21072000	-4.16310000	11.77507000
Au	-2.88429000	-1.66525000	11.77507000
Au	0.00000000	-1.66525000	11.77507000
Au	2.88429000	-1.66524000	11.77507000
Au	5.76857000	-1.66524000	11.77507000
Au	-4.32644000	0.83262000	11.77507000
Au	-1.44215000	0.83262000	11.77507000
Au	1.44214000	0.83263000	11.77507000
Au	4.32643000	0.83263000	11.77507000
Au	-5.76858000	3.33048000	11.77507000
Au	-2.88429000	3.33049000	11.77507000
Au	-0.00001000	3.33050000	11.77507000
Au	2.88428000	3.33050000	11.77507000
Au	0.00000000	0.00000000	14.13008000
Au	-1.44215000	2.49786000	14.13008000
Au	1.44214000	2.49786000	14.13008000
S	0.00706955	-1.96323379	15.36622849
H	-2.19287477	-0.28949822	16.16504125
H	2.94766834	-3.38113120	16.42563428
H	1.22420660	1.10524056	16.65087401
O	1.59234851	0.20928204	16.65969546
H	2.55320563	0.31234323	16.72611925
H	-4.17470491	1.06348106	16.84449429
C	-2.32308185	0.02238584	17.19777958
H	5.02696806	-4.43992546	17.30527477
C	3.20888818	-3.29876536	17.47723139
O	-0.75651267	-3.56625373	17.51187353
Mn	0.45649857	-1.59762889	17.54743998
C	-3.42937927	0.77787975	17.57856760
H	-1.69933270	-3.59942955	17.73168311
H	-0.38715453	-4.42212253	17.77528352
C	4.36992602	-3.88968273	17.96971793
N	-1.36497230	-0.36289212	18.06189341
N	2.35462419	-2.60286419	18.25108682
C	-3.54329956	1.14817467	18.91894386
H	-4.38942852	1.73583080	19.26096776
C	4.65353461	-3.74997583	19.32862652
C	-1.46886624	-0.00385145	19.36998875
C	2.62417502	-2.46340710	19.57725730
N	0.58968147	-1.19814472	19.66539731
H	5.54772621	-4.19299010	19.75568072
C	-2.55457623	0.75392309	19.82122076
C	3.77291094	-3.03140073	20.13802726
C	-0.36813052	-0.46433826	20.26756034
C	1.63211146	-1.67996287	20.37232475
H	-2.63804185	1.03745128	20.86309973
H	3.98749779	-2.91903165	21.19354418
C	-0.30655658	-0.18448968	21.63041901
C	1.74809332	-1.43434068	21.73898073
H	-1.09192218	0.38022868	22.11511141
H	2.60113076	-1.79882786	22.29634152
C	0.76802625	-0.66929844	22.40537685
H	-0.04172461	1.58787212	23.70723485
C	0.85622384	-0.38431285	23.84744764
C	0.36327066	0.82944072	24.37081845
H	1.75477246	-2.28691211	24.37782572

C	1.41448281	-1.32072802	24.73879049
C	0.42685193	1.09319023	25.73238826
C	1.47270796	-1.05455492	26.10524061
H	0.03979939	2.02050606	26.14098650
C	0.98829150	0.15909189	26.61805381
H	1.85696836	-1.82410226	26.76803296
C	0.95328619	0.51885589	28.08779152
H	2.60295926	-0.62993617	28.38821342
O	0.10533772	1.30926324	28.49289947
N	1.90149055	-0.08248494	28.86686946
H	3.89585872	-1.18267983	30.13509538
C	2.11213840	0.03806834	30.26558543
H	0.39956731	1.27450537	30.70871820
C	3.23424874	-0.62271677	30.79340393
C	1.25990371	0.76146686	31.11393356
C	3.50491732	-0.56430323	32.15826856
C	1.54607238	0.80915307	32.48078086
H	4.37509371	-1.07863248	32.55433430
C	2.65972300	0.15372976	33.01074415
H	0.88488602	1.36940778	33.13492452
S	3.00252486	0.23109514	34.75570876
Au	1.44214000	-4.16312000	36.01499000
Au	4.32643000	-4.16312000	36.01499000
Au	2.88428000	-1.66525000	36.01499000
Au	0.00000000	-4.99574000	38.37000000
Au	2.88429000	-4.99574000	38.37000000
Au	5.76858000	-4.99574000	38.37000000
Au	8.65287000	-4.99574000	38.37000000
Au	-1.44215000	-2.49788000	38.37000000
Au	1.44214000	-2.49788000	38.37000000
Au	4.32643000	-2.49788000	38.37000000
Au	7.21072000	-2.49788000	38.37000000
Au	-2.88429000	-0.00001000	38.37000000
Au	0.00000000	-0.00001000	38.37000000
Au	2.88429000	-0.00001000	38.37000000
Au	5.76858000	-0.00001000	38.37000000
Au	-4.32644000	2.49786000	38.37000000
Au	-1.44215000	2.49786000	38.37000000
Au	1.44214000	2.49786000	38.37000000
Au	4.32643000	2.49786000	38.37000000
Au	0.00000000	-3.33050000	40.72501000
Au	2.88429000	-3.33050000	40.72501000
Au	5.76857000	-3.33050000	40.72501000
Au	8.65286000	-3.33050000	40.72501000
Au	-1.44214000	-0.83263000	40.72501000
Au	1.44215000	-0.83263000	40.72501000
Au	4.32644000	-0.83263000	40.72501000
Au	7.21071000	-0.83263000	40.72501000
Au	-2.88429000	1.66523000	40.72501000
Au	0.00000000	1.66523000	40.72501000
Au	2.88429000	1.66523000	40.72501000
Au	5.76858000	1.66523000	40.72501000
Au	-4.32644000	4.16310000	40.72501000
Au	-1.44215000	4.16310000	40.72501000
Au	1.44214000	4.16310000	40.72501000
Au	4.32643000	4.16310000	40.72501000
Au	-1.44215000	-4.16312000	43.08002000
Au	1.44214000	-4.16312000	43.08002000

Au 4.32643000 -4.16312000 43.08002000
Au 7.21072000 -4.16312000 43.08002000
Au -2.88428000 -1.66526000 43.08002000
Au -0.00001000 -1.66525000 43.08002000
Au 2.88428000 -1.66525000 43.08002000
Au 5.76857000 -1.66525000 43.08002000
Au -4.32643000 0.83261000 43.08002000
Au -1.44214000 0.83261000 43.08002000
Au 1.44214000 0.83262000 43.08002000
Au 4.32643000 0.83262000 43.08002000
Au -5.76858000 3.33048000 43.08002000
Au -2.88429000 3.33048000 43.08002000
Au 0.00000000 3.33048000 43.08002000
Au 2.88428000 3.33048000 43.08002000
Au 0.00000000 -4.99574000 45.43504000
Au 2.88429000 -4.99574000 45.43504000
Au 5.76858000 -4.99574000 45.43504000
Au 8.65287000 -4.99574000 45.43504000
Au -1.44215000 -2.49788000 45.43504000
Au 1.44214000 -2.49788000 45.43504000
Au 4.32643000 -2.49788000 45.43504000
Au 7.21072000 -2.49788000 45.43504000
Au -2.88429000 -0.00001000 45.43504000
Au 0.00000000 -0.00001000 45.43504000
Au 2.88429000 -0.00001000 45.43504000
Au 5.76858000 -0.00001000 45.43504000
Au -4.32644000 2.49786000 45.43504000
Au -1.44215000 2.49786000 45.43504000
Au 1.44214000 2.49786000 45.43504000
Au 4.32643000 2.49786000 45.43504000
Au 0.00000000 -3.33050000 47.79005000
Au 2.88429000 -3.33050000 47.79005000
Au 5.76857000 -3.33050000 47.79005000
Au 8.65286000 -3.33050000 47.79005000
Au -1.44214000 -0.83263000 47.79005000
Au 1.44215000 -0.83263000 47.79005000
Au 4.32644000 -0.83263000 47.79005000
Au 7.21071000 -0.83263000 47.79005000
Au -2.88429000 1.66523000 47.79005000
Au 0.00000000 1.66523000 47.79005000
Au 2.88429000 1.66523000 47.79005000
Au 5.76858000 1.66523000 47.79005000
Au -4.32644000 4.16310000 47.79005000
Au -1.44215000 4.16310000 47.79005000
Au 1.44214000 4.16310000 47.79005000
Au 4.32643000 4.16310000 47.79005000
Au -1.44215000 -4.16312000 50.14506000
Au 1.44214000 -4.16312000 50.14506000
Au 4.32643000 -4.16312000 50.14506000
Au 7.21072000 -4.16312000 50.14506000
Au -2.88428000 -1.66526000 50.14506000
Au -0.00001000 -1.66525000 50.14506000
Au 2.88428000 -1.66525000 50.14506000
Au 5.76857000 -1.66525000 50.14506000
Au -4.32643000 0.83261000 50.14506000
Au -1.44214000 0.83261000 50.14506000
Au 1.44214000 0.83262000 50.14506000
Au 4.32643000 0.83262000 50.14506000

```
Au  -5.76858000   3.33048000  50.14506000
Au  -2.88429000   3.33048000  50.14506000
Au   0.00000000   3.33048000  50.14506000
Au   2.88428000   3.33048000  50.14506000
```

Sample input for TranSIESTA calculation: 0V calculation for Au-Mn-terpy-L1-Au

```
# Calcualtion Method

 SolutionMethod                transiesta

# SPECIES AND BASIS

 NumberOfAtoms         259
 NumberOfSpecies         7

 LatticeConstant        1.0000 Ang
 %block LatticeVectors
   11.53716000    0.000    0.00000
   -5.76858000   9.99147365    0.00000
   0.00000    0.00000  52.05007
 %endblock LatticeVectors

 #--BASIS SET

 PAO.BasisType split
 PAO.SplitNorm 0.15
 %block    PAO.BasisSizes
    Au  SZP
    S   DZP
    H   DZP
    O   DZP
    C   DZP
    Mn  DZP
    N   DZP
 %endblock  PAO.BasisSizes
 PAO.EnergyShift 0.01 eV

 # K-POINTS

 %block kgrid_Monkhorst_Pack
   10   0   0    0.0
    0  10   0    0.0
    0   0   1    0.0
 %endblock kgrid_Monkhorst_Pack
 BandLinesScale         ReciprocalLatticeVectors

 # GENERAL VARIABLES

 #--Exchange-correlation functionals
 XC.functional        GGA
 XC.authors           PBE
 MeshCutoff  250.0 Ry

# SCF OPTIONS
```

```
ElectronicTemperature          300 K
MaxSCFIterations              30000
DM.MixingWeight                0.02
DM.NumberPulay                 4        # Pulay convergency accelerator
#DM.MixSCF1                    T
#DM.MixH                      T
#DM.PulayOnFile                F       # Store in memory (F) or in files (T)
DM.Tolerance                  1.0D-5
DM.UseSaveDM                   T

# TRANSPORT VARIABLES

#-- ELECTRODES
TS.HSFileLeft   AuLeads.TSHS
TS.NumUsedAtomsLeft    48
TS.HSFileRight  AuLeads.TSHS
TS.NumUsedAtomsRight   48

#--TRANSPORT BLOCK
TS.TBT.NPoints        1000
TS.TBT.Emin          -1.0 eV
TS.TBT.Emax           1.0 eV
TS.TBT.OutputRegionData False
TS.BiasContour.NumPoints 100
TS.ComplexContour.Emin  -20.0 Ry
TS.ComplexContour.NumCircle 100
TS.ComplexContour.NumLine  20
TS.ComplexContour.NumPoles 10
TS.BiasContour.Eta 10D-4  Ry
TS.Voltage 0.000  eV

# SYSTEM

%block ChemicalSpeciesLabel
        1         79 Au    # Species index, atomic number, species label
        2         16 S     # Species index, atomic number, species label
        3          1 H     # Species index, atomic number, species label
        4          8 O     # Species index, atomic number, species label
        5          6 C     # Species index, atomic number, species label
        6         25 Mn    # Species index, atomic number, species label
        7          7 N     # Species index, atomic number, species label
%endblock ChemicalSpeciesLabel

AtomicCoordinatesFormat  Ang
%block AtomicCoordinatesAndAtomicSpecies
   0.00000000   -4.99573000    0.00000000   1  Au   1
   2.88429000   -4.99573000    0.00000000   1  Au   2
   5.76858000   -4.99573000    0.00000000   1  Au   3
   8.65286000   -4.99573000    0.00000000   1  Au   4
  -1.44214000   -2.49786000    0.00000000   1  Au   5
   1.44214000   -2.49786000    0.00000000   1  Au   6
   4.32643000   -2.49786000    0.00000000   1  Au   7
   7.21072000   -2.49786000    0.00000000   1  Au   8
  -2.88429000    0.00000000    0.00000000   1  Au   9
   0.00000000    0.00000000    0.00000000   1  Au  10
   2.88428000    0.00000000    0.00000000   1  Au  11
   5.76858000    0.00001000    0.00000000   1  Au  12
```

-4.32644000	2.49786000	0.00000000	1	Au	13
-1.44215000	2.49786000	0.00000000	1	Au	14
1.44214000	2.49786000	0.00000000	1	Au	15
4.32643000	2.49787000	0.00000000	1	Au	16
-0.00001000	-3.33049000	2.35502000	1	Au	17
2.88429000	-3.33049000	2.35502000	1	Au	18
5.76857000	-3.33049000	2.35502000	1	Au	19
8.65287000	-3.33048000	2.35502000	1	Au	20
-1.44215000	-0.83262000	2.35502000	1	Au	21
1.44214000	-0.83262000	2.35502000	1	Au	22
4.32643000	-0.83262000	2.35502000	1	Au	23
7.21072000	-0.83262000	2.35502000	1	Au	24
-2.88429000	1.66524000	2.35502000	1	Au	25
-0.00001000	1.66524000	2.35502000	1	Au	26
2.88429000	1.66525000	2.35502000	1	Au	27
5.76857000	1.66525000	2.35502000	1	Au	28
-4.32645000	4.16311000	2.35502000	1	Au	29
-1.44215000	4.16311000	2.35502000	1	Au	30
1.44213000	4.16311000	2.35502000	1	Au	31
4.32643000	4.16312000	2.35502000	1	Au	32
-1.44214000	-4.16312000	4.71004000	1	Au	33
1.44214000	-4.16312000	4.71004000	1	Au	34
4.32643000	-4.16310000	4.71004000	1	Au	35
7.21072000	-4.16310000	4.71004000	1	Au	36
-2.88429000	-1.66525000	4.71004000	1	Au	37
0.00000000	-1.66525000	4.71004000	1	Au	38
2.88429000	-1.66524000	4.71004000	1	Au	39
5.76857000	-1.66524000	4.71004000	1	Au	40
-4.32644000	0.83262000	4.71004000	1	Au	41
-1.44215000	0.83262000	4.71004000	1	Au	42
1.44214000	0.83263000	4.71004000	1	Au	43
4.32643000	0.83263000	4.71004000	1	Au	44
-5.76858000	3.33048000	4.71004000	1	Au	45
-2.88429000	3.33049000	4.71004000	1	Au	46
-0.00001000	3.33050000	4.71004000	1	Au	47
2.88428000	3.33050000	4.71004000	1	Au	48
0.00000000	-4.99573000	7.06505000	1	Au	49
2.88429000	-4.99573000	7.06505000	1	Au	50
5.76858000	-4.99573000	7.06505000	1	Au	51
8.65286000	-4.99573000	7.06505000	1	Au	52
-1.44214000	-2.49786000	7.06505000	1	Au	53
1.44214000	-2.49786000	7.06505000	1	Au	54
4.32643000	-2.49786000	7.06505000	1	Au	55
7.21072000	-2.49786000	7.06505000	1	Au	56
-2.88429000	0.00000000	7.06505000	1	Au	57
0.00000000	0.00000000	7.06505000	1	Au	58
2.88428000	0.00000000	7.06505000	1	Au	59
5.76858000	0.00001000	7.06505000	1	Au	60
-4.32644000	2.49786000	7.06505000	1	Au	61
-1.44215000	2.49786000	7.06505000	1	Au	62
1.44214000	2.49786000	7.06505000	1	Au	63
4.32643000	2.49787000	7.06505000	1	Au	64
-0.00001000	-3.33049000	9.42006000	1	Au	65
2.88429000	-3.33049000	9.42006000	1	Au	66
5.76857000	-3.33049000	9.42006000	1	Au	67
8.65287000	-3.33048000	9.42006000	1	Au	68
-1.44215000	-0.83262000	9.42006000	1	Au	69
1.44214000	-0.83262000	9.42006000	1	Au	70

4.32643000	-0.83262000	9.42006000	1	Au	71
7.21072000	-0.83262000	9.42006000	1	Au	72
-2.88429000	1.66524000	9.42006000	1	Au	73
-0.00001000	1.66524000	9.42006000	1	Au	74
2.88429000	1.66525000	9.42006000	1	Au	75
5.76857000	1.66525000	9.42006000	1	Au	76
-4.32645000	4.16311000	9.42006000	1	Au	77
-1.44215000	4.16311000	9.42006000	1	Au	78
1.44213000	4.16311000	9.42006000	1	Au	79
4.32643000	4.16312000	9.42006000	1	Au	80
-1.44214000	-4.16312000	11.77507000	1	Au	81
1.44214000	-4.16312000	11.77507000	1	Au	82
4.32643000	-4.16310000	11.77507000	1	Au	83
7.21072000	-4.16310000	11.77507000	1	Au	84
-2.88429000	-1.66525000	11.77507000	1	Au	85
0.00000000	-1.66525000	11.77507000	1	Au	86
2.88429000	-1.66524000	11.77507000	1	Au	87
5.76857000	-1.66524000	11.77507000	1	Au	88
-4.32644000	0.83262000	11.77507000	1	Au	89
-1.44215000	0.83262000	11.77507000	1	Au	90
1.44214000	0.83263000	11.77507000	1	Au	91
4.32643000	0.83263000	11.77507000	1	Au	92
-5.76858000	3.33048000	11.77507000	1	Au	93
-2.88429000	3.33049000	11.77507000	1	Au	94
-0.00001000	3.33050000	11.77507000	1	Au	95
2.88428000	3.33050000	11.77507000	1	Au	96
0.00000000	0.00000000	14.13008000	1	Au	97
-1.44215000	2.49786000	14.13008000	1	Au	98
1.44214000	2.49786000	14.13008000	1	Au	99
0.00284399	-1.88530461	15.48212233	2	S	100
2.64416995	-3.38431680	16.27177722	3	H	101
-2.40415828	-0.14095483	16.54282704	3	H	102
1.42900999	0.21584230	16.78704089	4	O	103
2.39500799	0.28109205	16.81482011	3	H	104
1.09518082	1.12223862	16.85978664	3	H	105
4.74075818	-4.55701004	16.94355415	3	H	106
2.97885795	-3.37351213	17.30558258	5	C	107
-4.29248000	1.22187034	17.43546506	3	H	108
-2.45469884	0.11203463	17.59848394	5	C	109
-0.97045798	-3.54049940	17.59875926	4	O	110
0.29283574	-1.60012343	17.66769299	6	Mn	111
4.14876409	-4.02751189	17.68182636	5	C	112
-0.59803136	-4.41022607	17.80609396	3	H	113
-1.89252442	-3.56406504	17.89442521	3	H	114
-3.50827779	0.87264652	18.09801371	5	C	115
2.20251586	-2.69953785	18.17530710	7	N	116
-1.45276306	-0.35047313	18.37046803	7	N	117
4.52704715	-3.97724285	19.02433000	5	C	118
5.43211728	-4.47183623	19.36266147	3	H	119
-3.51878312	1.16518430	19.46263974	5	C	120
2.56365717	-2.64721102	19.48580598	5	C	121
-1.45523027	-0.06840933	19.70131164	5	C	122
0.58029299	-1.33386458	19.77826363	7	N	123
-4.32074823	1.75449659	19.89599200	3	H	124
3.72799916	-3.28233081	19.93217583	5	C	125
-2.48414900	0.69129238	20.26920417	5	C	126
1.65163415	-1.88432183	20.38928407	5	C	127
-0.31074204	-0.61180136	20.49172506	5	C	128

4.01585227	-3.23934152	20.97520926	3	H	129
-2.48663715	0.91519468	21.32871132	3	H	130
1.86646211	-1.72349800	21.75325806	5	C	131
-0.15188451	-0.41667553	21.85840136	5	C	132
2.74714210	-2.14237522	22.22126263	3	H	133
-0.89126452	0.13638531	22.42149688	3	H	134
0.95863598	-0.97274720	22.53874217	5	C	135
1.15409998	-0.77767957	23.97319520	5	C	136
0.08420813	1.10899671	24.07958014	3	H	137
2.29015875	-2.60491627	24.30344881	3	H	138
0.61717136	0.34677008	24.63969341	5	C	139
1.88573300	-1.70328583	24.75309850	5	C	140
0.78938444	0.55509365	25.99843478	5	C	141
2.05448033	-1.51841441	26.11316993	5	C	142
0.37819761	1.42983200	26.48118650	3	H	143
2.59979893	-2.26114595	26.68923381	3	H	144
1.51351724	-0.38572915	26.76695406	5	C	145
1.73557973	-0.25615310	28.12765383	7	N	146
2.27369613	-0.99695980	28.55669990	3	H	147
0.44125671	1.57324385	28.62658464	4	O	148
1.23438644	0.72222822	29.00421738	5	C	149
3.57607369	-0.45028934	30.03406330	3	H	150
1.72099125	0.62877313	30.41133080	5	C	151
2.91760671	-0.01186162	30.77979028	5	C	152
0.02553574	1.75410035	31.10317673	3	H	153
0.93773442	1.24781123	31.39996554	5	C	154
3.31349945	-0.04394983	32.11731624	5	C	155
4.24521745	-0.52800907	32.39300929	3	H	156
1.33204445	1.20569637	32.73584086	5	C	157
2.51833011	0.55816659	33.09717326	5	C	158
0.71708650	1.67872319	33.49506109	3	H	159
3.02425236	0.51110683	34.80311231	2	S	160
1.44214000	-4.16312000	35.56499000	1	Au	161
4.32643000	-4.16312000	35.56499000	1	Au	162
2.88428000	-1.66525000	35.56499000	1	Au	163
0.00000000	-4.99574000	37.92000000	1	Au	164
2.88429000	-4.99574000	37.92000000	1	Au	165
5.76858000	-4.99574000	37.92000000	1	Au	166
8.65287000	-4.99574000	37.92000000	1	Au	167
-1.44215000	-2.49788000	37.92000000	1	Au	168
1.44214000	-2.49788000	37.92000000	1	Au	169
4.32643000	-2.49788000	37.92000000	1	Au	170
7.21072000	-2.49788000	37.92000000	1	Au	171
-2.88429000	-0.00001000	37.92000000	1	Au	172
0.00000000	-0.00001000	37.92000000	1	Au	173
2.88429000	-0.00001000	37.92000000	1	Au	174
5.76858000	-0.00001000	37.92000000	1	Au	175
-4.32644000	2.49786000	37.92000000	1	Au	176
-1.44215000	2.49786000	37.92000000	1	Au	177
1.44214000	2.49786000	37.92000000	1	Au	178
4.32643000	2.49786000	37.92000000	1	Au	179
0.00000000	-3.33050000	40.27501000	1	Au	180
2.88429000	-3.33050000	40.27501000	1	Au	181
5.76857000	-3.33050000	40.27501000	1	Au	182
8.65286000	-3.33050000	40.27501000	1	Au	183
-1.44214000	-0.83263000	40.27501000	1	Au	184
1.44215000	-0.83263000	40.27501000	1	Au	185
4.32644000	-0.83263000	40.27501000	1	Au	186

7.21071000	-0.83263000	40.27501000	1	Au 187
-2.88429000	1.66523000	40.27501000	1	Au 188
0.00000000	1.66523000	40.27501000	1	Au 189
2.88429000	1.66523000	40.27501000	1	Au 190
5.76858000	1.66523000	40.27501000	1	Au 191
-4.32644000	4.16310000	40.27501000	1	Au 192
-1.44215000	4.16310000	40.27501000	1	Au 193
1.44214000	4.16310000	40.27501000	1	Au 194
4.32643000	4.16310000	40.27501000	1	Au 195
-1.44215000	-4.16312000	42.63002000	1	Au 196
1.44214000	-4.16312000	42.63002000	1	Au 197
4.32643000	-4.16312000	42.63002000	1	Au 198
7.21072000	-4.16312000	42.63002000	1	Au 199
-2.88428000	-1.66526000	42.63002000	1	Au 200
-0.00001000	-1.66525000	42.63002000	1	Au 201
2.88428000	-1.66525000	42.63002000	1	Au 202
5.76857000	-1.66525000	42.63002000	1	Au 203
-4.32643000	0.83261000	42.63002000	1	Au 204
-1.44214000	0.83261000	42.63002000	1	Au 205
1.44214000	0.83262000	42.63002000	1	Au 206
4.32643000	0.83262000	42.63002000	1	Au 207
-5.76858000	3.33048000	42.63002000	1	Au 208
-2.88429000	3.33048000	42.63002000	1	Au 209
0.00000000	3.33048000	42.63002000	1	Au 210
2.88428000	3.33048000	42.63002000	1	Au 211
0.00000000	-4.99574000	44.98504000	1	Au 212
2.88429000	-4.99574000	44.98504000	1	Au 213
5.76858000	-4.99574000	44.98504000	1	Au 214
8.65287000	-4.99574000	44.98504000	1	Au 215
-1.44215000	-2.49788000	44.98504000	1	Au 216
1.44214000	-2.49788000	44.98504000	1	Au 217
4.32643000	-2.49788000	44.98504000	1	Au 218
7.21072000	-2.49788000	44.98504000	1	Au 219
-2.88429000	-0.00001000	44.98504000	1	Au 220
0.00000000	-0.00001000	44.98504000	1	Au 221
2.88429000	-0.00001000	44.98504000	1	Au 222
5.76858000	-0.00001000	44.98504000	1	Au 223
-4.32644000	2.49786000	44.98504000	1	Au 224
-1.44215000	2.49786000	44.98504000	1	Au 225
1.44214000	2.49786000	44.98504000	1	Au 226
4.32643000	2.49786000	44.98504000	1	Au 227
0.00000000	-3.33050000	47.34005000	1	Au 228
2.88429000	-3.33050000	47.34005000	1	Au 229
5.76857000	-3.33050000	47.34005000	1	Au 230
8.65286000	-3.33050000	47.34005000	1	Au 231
-1.44214000	-0.83263000	47.34005000	1	Au 232
1.44215000	-0.83263000	47.34005000	1	Au 233
4.32644000	-0.83263000	47.34005000	1	Au 234
7.21071000	-0.83263000	47.34005000	1	Au 235
-2.88429000	1.66523000	47.34005000	1	Au 236
0.00000000	1.66523000	47.34005000	1	Au 237
2.88429000	1.66523000	47.34005000	1	Au 238
5.76858000	1.66523000	47.34005000	1	Au 239
-4.32644000	4.16310000	47.34005000	1	Au 240
-1.44215000	4.16310000	47.34005000	1	Au 241
1.44214000	4.16310000	47.34005000	1	Au 242
4.32643000	4.16310000	47.34005000	1	Au 243
-1.44215000	-4.16312000	49.69506000	1	Au 244

```
  1.44214000   -4.16312000   49.69506000   1  Au 245
  4.32643000   -4.16312000   49.69506000   1  Au 246
  7.21072000   -4.16312000   49.69506000   1  Au 247
 -2.88428000   -1.66526000   49.69506000   1  Au 248
 -0.00001000   -1.66525000   49.69506000   1  Au 249
  2.88428000   -1.66525000   49.69506000   1  Au 250
  5.76857000   -1.66525000   49.69506000   1  Au 251
 -4.32643000    0.83261000   49.69506000   1  Au 252
 -1.44214000    0.83261000   49.69506000   1  Au 253
  1.44214000    0.83262000   49.69506000   1  Au 254
  4.32643000    0.83262000   49.69506000   1  Au 255
 -5.76858000    3.33048000   49.69506000   1  Au 256
 -2.88429000    3.33048000   49.69506000   1  Au 257
  0.00000000    3.33048000   49.69506000   1  Au 258
  2.88428000    3.33048000   49.69506000   1  Au 259
%endblock AtomicCoordinatesAndAtomicSpecies
```